bioRxiv preprint doi: https://doi.org/10.1101/2021.05.25.445613; this version posted May 25, 2021. The copyright holder for this preprint (which was not certified by peer review) is the author/funder. All rights reserved. No reuse allowed without permission.

Loss-of-function variants in the schizophrenia risk gene *SETD1A* alter neuronal network activity in human neurons through cAMP/PKA pathway

S. Wang[1], J.R. van Rhijn[1], I. Akkouh[2, 3], N. Kogo[4, 5], N. Maas[1], A. Bleeck[1], E. Lewerissa[4], K. Wu[4], C. Schoenmaker[4], S. Djurovic[2, 6], H. van Bokhoven[1, 4], T. Kleefstra[4], N. Nadif Kasri[1, 4, #], D. Schubert[1, #]

1. Department of Cognitive Neurosciences, Radboudumc, Donders Institute for Brain Cognition and Behaviour , Nijmegen (the Netherlands)
2. Department of Medical Genetics, Oslo University Hospital, Oslo (Norway)
3. NORMENT, Institute of Clinical Medicine, University of Oslo, Oslo, (Norway)
4. Department of Human Genetics, Radboudumc, Donders Institute for Brain Cognition and Behaviour, Nijmegen (the Netherlands)
5. Department of Biophysics, Donders Institute for Brain Cognition and Behaviour, Nijmegen (the Netherlands)
6. NORMENT, Department of Clinical Science, University of Bergen, Bergen, (Norway)

[#] Co-last author.

Corresponding author: Dirk Schubert

Email: d.schubert@donders.ru.nl

Dept. Cognitive Neuroscience

Donders Institute for Brain, Cognition and Behaviour

Radboud University Nijmegen Medical Centre

Postbus 9101

6500 HB Nijmegen

The Netherlands

Phone: +31 24 3615039

bioRxiv preprint doi: https://doi.org/10.1101/2021.05.25.445613; this version posted May 25, 2021. The copyright holder for this preprint (which was not certified by peer review) is the author/funder. All rights reserved. No reuse allowed without permission.

Abstract

Heterozygous loss-of-function (LoF) mutations in *SETD1A*, which encodes a subunit of histone H3 lysine 4 methyltransferase, have been shown to cause a novel neurodevelopmental syndrome and increase the risk for schizophrenia. To study the effect of decreased SETD1A function in human cells, we generated excitatory/inhibitory neuronal networks from human induced pluripotent stem cells with a *SETD1A* heterozygous LoF mutation (*SETD1A*$^{+/-}$). Our data show that *SETD1A* haploinsufficiency resulted in altered neuronal network activity, which was mainly characterized by an overly synchronized network. In individual neurons, this network phenotype was reflected by increased somatodendritic complexity and elevated synaptic connectivity. We found that this network phenotype was driven by *SETD1A* haploinsufficiency in glutamatergic neurons. In accordance with the functional changes, transcriptomic profiling revealed perturbations in gene sets associated with schizophrenia, synaptic transmission and glutamatergic synaptic function. At the molecular level, we identified specific changes in the cAMP/PKA pathway pointing toward a hyperactive cAMP pathway in *SETD1A*$^{+/-}$ neurons. Finally, using pharmacological experiments targeting the cAMP pathway we were able to rescue the network deficits in *SETD1A*$^{+/-}$ cultures. In conclusion, our results illuminate key molecular, cellular and network abnormalities caused by *SETD1A* haploinsufficiency and demonstrate a direct link between SETD1A and the cAMP-dependent pathway in human neurons.

bioRxiv preprint doi: https://doi.org/10.1101/2021.05.25.445613; this version posted May 25, 2021. The copyright holder for this preprint (which was not certified by peer review) is the author/funder. All rights reserved. No reuse allowed without permission.

Introduction

Schizophrenia (SCZ) is a complex and heterogeneous syndrome with poorly defined neurobiology. It is a highly heritable disease (~80% heritability) with a substantial genetic component[1–3]. In the past decade, considerable progress has been made to better understand the genetic burden related to SCZ. Genetic loci related to SCZ can either be common variants, which typically exert small effects, or rare variants, which can result in a large effect on individual risk[4]. One of the genes with such rare large-effect size variants is *SETD1A,* encoding SET domain-containing protein 1A. Accumulating studies demonstrate that loss-of-function (LoF) and missense mutations in *SETD1A* are associated with SCZ[5–7], but also found in individuals with disrupted speech development[8] and early-onset epilepsy[9]. Furthermore, we presented a series of de novo *SETD1A* heterozygous LoF mutations and defined a novel neurodevelopmental syndrome based on a cohort of 15 individuals (age ranging from 34 months to 23 years old)[10]. The core characteristics of these individuals include global developmental delay (such as speech delay or motor delay) and/or intellectual disability, facial dysmorphisms as well as behavior and psychiatric abnormalities, including psychotic episodes. In addition, abnormalities in brain structure, visual and hearing impairments have also been reported in some of these individuals[10]. *SETD1A* mutations thus appear to cause biological vulnerability to a broad neurodevelopmental phenotypic spectrum.

SETD1A encodes a subunit of the human Set/COMPASS complex, which methylates histone H3 at position lysine-4 (H3K4me1, H3K4me2, H3K4me3) and participates in the regulation of gene expression. Mouse models with heterozygous LoF mutation of *Setd1a* (*Setd1a*$^{+/-}$) recapitulate SCZ-related behavioral abnormalities, such as deficits in working memory and social interaction[11, 12]. At the cellular level, *Setd1a*$^{+/-}$ mice display reduced axon branches and dendritic spines, increased neuronal excitability[11] as well as impaired excitatory synaptic neurotransmission[12]. Furthermore, *Setd1a*$^{+/-}$ mice show an altered transcriptomic profile in the medial prefrontal cortex (mPFC), a highly relevant region for SCZ[11]. In other brain regions, such as visual cortex (V1),

bioRxiv preprint doi: https://doi.org/10.1101/2021.05.25.445613; this version posted May 25, 2021. The copyright holder for this preprint (which was not certified by peer review) is the author/funder. All rights reserved. No reuse allowed without permission.

Setd1a$^{+/-}$ mice exhibit aberrant ensemble activity and gamma oscillations[13]. All of these studies suggest *SETD1A* haploinsufficiency results in neuronal circuit dysfunction. However, the exact cellular and molecular mechanisms of how *SETD1A* mutations lead to disrupted neuronal connectivity causing such severe mental symptoms, especially in a human context, remain poorly understood.

To investigate the role of SETD1A in neuronal network development and synaptic organization, we generated an isogenic human induced pluripotent stem cell (hiPSC) line with *SETD1A* haploinsufficiency through CRISPR/Cas9. Subsequently, hiPSCs were differentiated into homogenous populations of glutamatergic and GABAergic neurons[14]. In *in vitro* cultures containing defined compositions of glutamatergic and GABAergic neurons, we comprehensively analyzed molecular, structural and functional neuronal properties from single cells and neuronal networks during development. The results presented here demonstrate that *SETD1A* haploinsufficiency leads to key morphological, electrophysiological and transcriptional alterations. At molecular level, we show that the *SETD1A*$^{+/-}$ network phenotype is mediated by upregulated cyclic adenosine monophosphate (cAMP)/PKA pathway. This has been further confirmed by showing that pharmacological inhibition of cAMP/PKA rescues the *SETD1A*$^{+/-}$ network phenotype. Therefore, our results reveal cAMP/PKA as a potential downstream pathway affected by *SETD1A* mutation, opening novel therapeutics opportunities for patients carrying *SETD1A* variant.

Results

SETD1A$^{+/-}$ neuronal networks exhibit dysregulated functional organization.

We used CRISPR/Cas9 to generate an isogenic hiPSC line with a heterozygous LoF mutation of *SETD1A* by targeting exon 7 of *SETD1A* in a healthy hiPSC line[15] **(Figure 1a)**. We introduced a frameshift mutation in exon 7 leading to a LoF of the protein, mimicking a mutation reported in an individual diagnosed with SCZ[5]. Two clones with indels in *SETD1A* were selected for further characterization, which carry 28 (clone 1) and 8 (clone 2) base pairs (bp) deletions on one allele, respectively **(Figure S1a)**,

bioRxiv preprint doi: https://doi.org/10.1101/2021.05.25.445613; this version posted May 25, 2021. The copyright holder for this preprint (which was not certified by peer review) is the author/funder. All rights reserved. No reuse allowed without permission.

both predicting a premature stop codon. SETD1A mRNA and protein levels were approximately halved in both *SETD1A*$^{+/-}$ hiPSC clones, indicating that both variants represent LoF alleles **(Figure 1b-c, S1b)**. The pluripotency of selected clones was not affected by the CRISPR/Cas9 editing **(Figure S1c)**.

Disrupted neuronal connectivity has been reported in SCZ patients and animal models of SCZ[16]. We evaluated whether LoF of *SETD1A* gene results in neuronal network impairment *in vitro*. To this end, we generated composite networks of glutamatergic (~75%) and GABAergic (~25%) neurons (excitatory/inhibitory cultures, E/I cultures) comprised of either control or *SETD1A*$^{+/-}$ hiPSCs, by forced expression of the transcription factor *Ngn2* or *Ascl1,* respectively, as recently described (**Figure 1d**)[14]. We did not detect any significant differences in the percentage of glutamatergic or GABAergic neurons between control and *SETD1A*$^{+/-}$ networks at days *in vitro* (DIV) 49 (**Figure 1e, S2a**). Moreover, following acute treatment with 100 µM Picrotoxin (PTX) at DIV49 on micro-electrode array (MEA), both mean firing rate and network burst duration went up for both control and *SETD1A*$^{+/-}$ networks (**Figure S2b-c**), indicating that at DIV49 GABAergic neurons exhibit robust inhibitory control[14].

In order to assess if neuronal network activity differs between control and *SETD1A*$^{+/-}$ E/I cultures during development, we used MEA recordings[17] (**Figure S2b**). We recorded neuronal network activity once a week from DIV21 to DIV49. After 3 weeks of differentiation, both control and *SETD1A*$^{+/-}$ networks showed network burst activity **(Figure 1f)**, which indicates the neurons are functionally connected and integrated into a network. Network burst activity increased during development for both groups, and plateaued at around DIV42. Strikingly, *SETD1A*$^{+/-}$ networks showed a significantly increased network burst activity compared to control from DIV21 to DIV49, accompanied by a shorter network inter burst interval, a decrease in network burst duration as well as lower spike rate within a burst **(Figure 1g, S2d)**. Interestingly, the global activity (i.e., mean firing rate, **Figure 1g**) was similar between control and *SETD1A*$^{+/-}$ networks, which implies there was a re-organization of network connectivity in *SETD1A*$^{+/-}$ E/I cultures, rather than general hyperactivity. Calcium

bioRxiv preprint doi: https://doi.org/10.1101/2021.05.25.445613; this version posted May 25, 2021. The copyright holder for this preprint (which was not certified by peer review) is the author/funder. All rights reserved. No reuse allowed without permission.

imaging further confirmed the increased synchronized activity in *SETD1A*$^{+/-}$ networks **(Figure S3a-d)**.

We next evaluated if this network re-organization in *SETD1A*$^{+/-}$ E/I cultures is related to changes in intrinsic properties and/or synaptic inputs using single-cell patch clamp. Intrinsic properties were similar between control and *SETD1A*$^{+/-}$ neurons at both DIV21 and DIV49 **(Figure S4, Table S1)**, in glutamatergic and GABAergic neurons. We additionally measured general synaptic integration by recording spontaneous postsynaptic currents (sPSCs). Neither sPSC frequency nor amplitude were different between control and *SETD1A*$^{+/-}$ cultures at DIV21 or DIV49 **(Figure 1h, Table S1)**. However, we did observe that the frequency of temporally correlated bursts of synaptic inputs (sPSC bursts) onto the postsynaptic neuron was significantly increased at DIV49 in *SETD1A*$^{+/-}$ E/I cultures, both in glutamatergic and GABAergic neurons **(Figure 1i**). This is in line with the increased network burst rate at the population level shown in the MEA recordings and confirms that reduced SETD1A expression results in increased network activity. Since analysis of sPSC reflects network activity rather than yield quantitative information regarding synaptic connectivity, we next measured miniature postsynaptic currents (mPSCs), which are action-potential independent and can be indicative for the reorganization of synaptic inputs, altered synapse numbers, and changes in release probabilities (mPSC frequency) and receptor abundance (mPSC amplitude). Both mPSC frequency and amplitude were significantly increased in both glutamatergic and GABAergic *SETD1A*$^{+/-}$ neurons at DIV49 (**Figure 1j**). This suggests that networks comprised of *SETD1A*$^{+/-}$ neurons not only exhibit increased network activity but also elevated synaptic connectivity, and this could be a major contributor to the network phenotype we observed at the population level.

SETD1A$^{+/-}$ neurons show aberrant somatodendritic morphology.

Based on the MEA results, we next sought to investigate whether *SETD1A*$^{+/-}$ neurons exhibit changes in dendritic morphology and/or synapse formation. At DIV21, control and *SETD1A*$^{+/-}$ E/I cultures did not differ from each other in any of the morphological

bioRxiv preprint doi: https://doi.org/10.1101/2021.05.25.445613; this version posted May 25, 2021. The copyright holder for this preprint (which was not certified by peer review) is the author/funder. All rights reserved. No reuse allowed without permission.

parameters for both glutamatergic and GABAergic neurons **(Figure 2a-b, e-f)**. However, at DIV49, *SETD1A*$^{+/-}$ neurons displayed a significantly larger soma size, accompanied by a longer dendritic length, more dendritic branches and a larger covered area for both glutamatergic and GABAergic neurons **(Figure 2c-f)**. Finally, we performed a Sholl analysis and confirmed that there were no significant differences in the distribution of dendritic length at DIV21 for both neuronal types **(Figure 2a-b)**, whereas at DIV49, the dendritic length at multiple distances from the soma was significantly longer in both glutamatergic and GABAergic *SETD1A*$^{+/-}$ neurons **(Figure 2c-d)**. These results collectively indicate that *SETD1A* haploinsufficiency leads to a more complex somatodendritic morphology, but this only becomes significant during later developmental stages.

To measure synapse formation, we immunostained neurons for pre- and postsynaptic markers (Synapsin and Homer1 for glutamatergic synapses, VGAT and Gephyrin for GABAergic synapses). We found no differences in the density of Synapsin/Homer1 or VGAT/Gephyrin co-localised puncta between both genotypes at both DIV21 and DIV49 **(Figure 2g-h)**. These data, combined with the observation that all *SETD1A*$^{+/-}$ neurons show a longer dendritic length at DIV49, imply that the total amount of synapses per neuron is higher in *SETD1A*$^{+/-}$ neurons, which is reflected by the increase in mPSC frequency at DIV49 **(Figure 1j).**

SETD1A haploinsufficiency leads to an altered transcriptomic profile.

To identify the molecular perturbations that underlie the network phenotypes caused by *SETD1A* haploinsufficiency, we conducted RNA-seq at DIV49. Principal component analysis (PCA) of transcriptional profiles exhibited clear clustering of biological replicates per genotype **(Figure 3a)**. We quantified the differentially expressed genes (DEGs) and found that 380 genes were downregulated and 539 genes were upregulated in *SETD1A*$^{+/-}$ E/I cultures compared with control cultures **(Figure 3b)**. Interestingly, when we performed a disease enrichment analysis using the DisGeNET database which consists of more than 10,000 disorders[18], SCZ was identified as the top hit **(Figure 3c, Table S2)**. This indicates that *SETD1A*

bioRxiv preprint doi: https://doi.org/10.1101/2021.05.25.445613; this version posted May 25, 2021. The copyright holder for this preprint (which was not certified by peer review) is the author/funder. All rights reserved. No reuse allowed without permission.

haploinsufficiency in our model captures some key genetic alterations typically linked to SCZ. In addition, we conducted Gene Ontology (GO) analysis to examine which biological functions are over-represented in the DEGs. Significant enrichment in GO terms relevant to "synaptic function", "morphogenesis", "ion channels" and "learning and memory" were identified **(Figure 3d, Table S3)**. Proteins encoded by these genes interact with each other as indicated in the protein-protein interaction analysis generated through STRING[19] **(Figure 3e)**. Interestingly, we noticed that many GO terms and DEGs relevant to glutamatergic neurons were identified, such as "glutamate receptor binding", "glutamate receptor signaling pathway" and "glutamatergic synapse" **(Figure 3d-f)**. This is consistent with the data from *Setd1a*$^{+/-}$ mouse models, where it was shown that SETD1A target genes are highly expressed in pyramidal neurons[11]. This also suggests that the altered network phenotype caused by *SETD1A* haploinsufficiency might be driven predominantly by perturbations in glutamatergic neurons.

To explore the cross-species validity of the SETD1A target genes, we compared our DEGs list with the published transcriptome of *Setd1a*$^{+/-}$ mouse model from Mukai et al[11], and found in total 11 overlapping genes **(Table S4)**. One of these genes is *SLITRK4,* the gene showing the strongest upregulation in *SETD1A*$^{+/-}$ cultures (**Figure 3b**), which is involved in neurite outgrowth[20]. Furthermore, we found a significant association between our DEGs and 78 SFARI genes (Fisher's exact: $p=1.1e^{-5}$), an autism-related genes database **(Table S5)**. This is in line with the suggested genetic overlap between SCZ and autism[21]. Taken together, these results indicate that transcription is profoundly disturbed in *SETD1A*$^{+/-}$ neurons and DEGs are enriched in specific gene sets related to SCZ and synaptic function, especially the ones relevant for glutamatergic synapse function.

SETD1A$^{+/-}$ glutamatergic neuronal cultures recapitulate the *SETD1A*$^{+/-}$ E/I network phenotype

Our RNA-seq results clearly establish a link between *SETD1A* haploinsufficiency and glutamatergic synapse function. We therefore hypothesized that glutamatergic

bioRxiv preprint doi: https://doi.org/10.1101/2021.05.25.445613; this version posted May 25, 2021. The copyright holder for this preprint (which was not certified by peer review) is the author/funder. All rights reserved. No reuse allowed without permission.

neurons might be the main contributor to the network phenotype in *SETD1A*$^{+/-}$ E/I cultures. To test this hypothesis, we set up homogeneous glutamatergic neuronal cultures **(Figure 4a)**. We measured the glutamatergic neuronal network activity on MEA between DIV21 to DIV49 **(Figure 4b)**. Consistent with the phenotype of E/I networks, *SETD1A*$^{+/-}$ glutamatergic neuronal networks exhibited significantly higher burst activity while decreased burst duration and burst spike rate at DIV49. Global activity (i.e. mean firing rate) did not differ between two groups **(Figure 4c)**. Next, we investigated if in glutamatergic cultures, there might be differences between control and *SETD1A*$^{+/-}$ neurons at the single cell level **(Figure 4g-k, S7, Table S6)**. Similar to the E/I cultures, we observed an increased sPSC burst rate at the single cell level in particular at DIV49 **(Figure 4j-k, Table S6)**. Taken together, our data show that E/I cultures and glutamatergic cultures are similarly affected when SETD1A expression is reduced. This was further supported by the observation that in glutamatergic neuronal networks, *SETD1A*$^{+/-}$ neurons showed a similar increase in morphological complexity as in the E/I cultures **(Figure 4d-f, S6a-d)**. Finally, we performed a transcriptome analysis for glutamatergic cultures at DIV49. We identified in total 455 DEGs, with 177 downregulated and 278 upregulated genes **(Figure S5a-b)**. Notably, we again identified *SLITRK4* as a top hit **(Figure S5b)**. Enrichment analysis detected GO terms such as “glutamatergic synapse”, “synapse organization”, “synapse assembly”, and many others related to synaptic function **(Figure S5d-f)**. In disease association analysis, we found “bipolar disorder” and “SCZ” within the top hits **(Figure S5c)**. Overall, *SETD1A*$^{+/-}$ glutamatergic cultures recapitulate the network phenotype observed in the E/I cultures, indicating that SETD1A plays a major role in glutamatergic neurons.

SETD1A haploinsufficiency leads to activation of cAMP/PKA/CREB pathway

The changes in neuronal network activity observed in *SETD1A*$^{+/-}$ cultures (E/I and glutamatergic cultures) suggest that pathways related to regulation of neuronal activity could be affected. Interestingly, in our transcriptome data we found that the upregulated DEGs were enriched in several annotations related to second messenger

bioRxiv preprint doi: https://doi.org/10.1101/2021.05.25.445613; this version posted May 25, 2021. The copyright holder for this preprint (which was not certified by peer review) is the author/funder. All rights reserved. No reuse allowed without permission.

signaling, such as “G protein-coupled receptor signaling pathway, coupled to cyclic nucleotide second messenger”, “second-messenger-mediated signaling”, and “adenylate cyclase-modulating G protein-coupled receptor signaling pathway” **(Figure 5a, Table S7)**. In agreement with this finding, we found that multiple enzymes involved in the synthesis and degradation of cAMP were dysregulated, both in the E/I and glutamatergic cultures. Specifically, genes coding for proteins involved in cAMP production (*ADCY2, ADCY3* and *ADCY8)*[22–24] were significantly upregulated, whereas genes encoding for phosphodiesterases (*PDE12, PDE7a* and *PDE1a*), important for cAMP degradation[25–27], were downregulated **(Figure 5b)**. This strongly suggests that the cAMP pathway is hyperactive in *SETD1A*$^{+/-}$ neurons.

To test this hypothesis, we measured the phosphorylation of cAMP-response element binding protein (pCREB), which is a downstream signaling protein in the cAMP/PKA pathway[28] **(Figure 5c)**. We immunostained neurons for anti-pCREB, an antibody detecting endogenous levels of CREB only when phosphorylated at serine[133]. As a positive control, we stimulated the cAMP pathway on control E/I cultures with 10 µM forskolin (FSK), a well-known adenylyl cyclase (AC) agonist and PKA/CREB pathway activator[29–31]. As expected, FSK significantly increased the level of pCREB in control neurons. In addition, we found that the level of pCREB in *SETD1A*$^{+/-}$ neurons was significantly higher compared to control neurons **(Figure 5d-e)**. This result supports our hypothesis that the cAMP/PKA/CREB pathway exhibits increased activity in *SETD1A*$^{+/-}$ neurons.

To investigate the link between enhanced cAMP activation and the neuronal network phenotype observed in *SETD1A*$^{+/-}$ neurons further, we bidirectionally modulated cAMP levels in control or *SETD1A*$^{+/-}$ neurons. Interestingly, we found that acute stimulation of control neurons with 10 µM FSK for 1 hour resulted in an increase in network bust rate, with a parallel reduction in inter network burst interval **(Figure 5f-g, S8a-c)**, mimicking the network phenotype of *SETD1A*$^{+/-}$ E/I cultures. In addition, burst spike rate and network burst duration were decreased, although the difference was

bioRxiv preprint doi: https://doi.org/10.1101/2021.05.25.445613; this version posted May 25, 2021. The copyright holder for this preprint (which was not certified by peer review) is the author/funder. All rights reserved. No reuse allowed without permission.

not significant **(Figure S8c)**. These results show that control networks treated with forskolin resemble *SETD1A*$^{+/-}$ neuronal networks. In a second set of experiments, we examined whether blocking cAMP using AC inhibitor SQ22536 in *SETD1A*$^{+/-}$ networks would be sufficient to normalize the phenotype caused by *SETD1A* haploinsufficiency to control levels. Indeed, after 8 days of treatment with 100 µM SQ22536, we found that the major network parameters were normalized, including the network burst rate **(Figure 5h-i, S9a-b).** We next investigated whether direct manipulation of the PKA pathway, which is a downstream target of cAMP, could also normalize *SETD1A*$^{+/-}$ network activity to control levels. Two independent chemical inhibitors of PKA, H89 and KT5720[32, 33], were applied to *SETD1A*$^{+/-}$ networks at DIV51 on MEA. After one hour treatment with either H89 (2 µM) or KT5720 (1 µM) in *SETD1A*$^{+/-}$ networks, the major network parameters were normalized, including the network burst rate **(Figure 5j-k, S10a-c)**. Taken together, our results suggest that cAMP/PKA is the main molecular pathway through which *SETD1A* haploinsufficiency leads to key neuronal network alteration.

bioRxiv preprint doi: https://doi.org/10.1101/2021.05.25.445613; this version posted May 25, 2021. The copyright holder for this preprint (which was not certified by peer review) is the author/funder. All rights reserved. No reuse allowed without permission.

Discussion

Heterozygous LoF variants in *SETD1A*, with high penetrance for SCZ, provides a unique opportunity to investigate early neuronal dysfunction that might underlie the increased vulnerability to SCZ. Here, we reveal crucial molecular signatures and neurodevelopmental abnormalities caused by *SETD1A* haploinsufficiency in human neurons. We show that *SETD1A* haploinsufficiency leads to altered neuronal network organization, governed predominantly by changes in glutamatergic neuronal function. Furthermore, we identify increased cAMP/PKA activity as a key contributor to the functional phenotype of *SETD1A*$^{+/-}$ networks.

One major consistent characteristic of hiPSC-derived *SETD1A*$^{+/-}$ networks is the increased network burst rate, which is reflected by an increase in synaptic connectivity at the single cell level. Synchronized burst activity plays an important role during early brain development[34] and is considered to be a fundamental mechanism for information processing, hence relevant for perception, memory and cognition[35]. Intriguingly, abnormalities in neural synchronization *in vivo*, which reflect neural circuit dysfunction, are suggested as one of the core pathophysiological mechanisms in SCZ[36, 37]. For example, increased oscillatory synchronization is found to be correlated with positive symptoms of SCZ[38, 39], while both increased and reduced oscillations are associated with negative symptoms[37, 40]. In the primary visual cortex of *Setd1a*$^{+/-}$ mice, Hamm et al identified reduced oscillations, providing circuit-level insight into the underlying neurobiology of sensory-processing abnormality seen in SCZ[13]. In this regard, both our human *in vitro* model and mouse model showed aberrant synchronized activity at different developmental stages, suggesting circuit disruption caused by *SETD1A* haploinsufficiency.

Disrupted glutamatergic signaling plays a critical role in the pathogenesis of SCZ[41]. Consistently, on several levels, our data provide evidence supporting the idea that glutamatergic neurons are the main contributors for the network phenotype caused by *SETD1A* haploinsufficiency. First, through transcriptional profiling of *SETD1A*$^{+/-}$ E/I

bioRxiv preprint doi: https://doi.org/10.1101/2021.05.25.445613; this version posted May 25, 2021. The copyright holder for this preprint (which was not certified by peer review) is the author/funder. All rights reserved. No reuse allowed without permission.

cultures, we identified a genetic signature suggestive of perturbed function of glutamatergic signaling. Dysregulated genes include the ones encoding for metabotropic glutamate receptors (*GRM4, GRM3*), ionotropic glutamate receptors subunits (*GRIK3, GRIN2A*), as well as proteins involved in glutamatergic signaling (*SHISA6, SHISA7, CAMK4, PSD93, VAMP1*). This is in line with the previous finding that target genes of SETD1A were mainly expressed in pyramidal neurons[11]. Furthermore, in L2/3 pyramidal neurons from the mPFC of *Setd1a*$^{+/-}$ mice, only excitatory synaptic transmission was altered, whereas inhibitory synaptic transmission remained unchanged[12]. Second, measurements from single-cell electrophysiology and MEA with homogenous glutamatergic neurons show the same network signature as observed in E/I networks, indicating glutamatergic neurons are the main driving factor in this phenotype. Third, similar to E/I cultures, we identified a more complex somatodendritic morphology in glutamatergic cultures, which provides the basis for the formation of the altered network circuits. Fourth, from both E/I and glutamatergic cultures, transcriptomic data highlight a striking upregulation of *SLITRK4*, a pyramidal neuron-specific gene[11] involved in neurite outgrowth and synaptogenesis[20]. Moreover, it has been shown that variants in *SLITRK4* are associated with neuropsychiatric disorders, such as schizophrenia[42, 43]. *SLITRK4* has also been identified as a DEG from *Setd1a*$^{+/-}$ mice[11], emphasizing its important role as a downstream target of SETD1A across species. Overall, these results reveal that SETD1A plays an essential role in the function of glutamatergic neurons.

Our data identify several molecular mechanisms that contribute to the increased network burst frequency in *SETD1A*$^{+/-}$ networks. Functional output of a neuron can be mediated by two fundamental components: intrinsic excitability and synaptic strength[44]. Based on our single-cell data, intrinsic excitability of both glutamatergic and GABAergic *SETD1A*$^{+/-}$ neurons is unaltered. This is consistent with the previous finding that neuronal excitability was unchanged in L2/3 pyramidal neurons from mPFC of *Setd1a*$^{+/-}$ mice[12]. We thus inferred there could be changed synaptic strength of *SETD1A*$^{+/-}$ neurons. Our transcriptomic data suggested *SETD1A* haploinsufficiency

bioRxiv preprint doi: https://doi.org/10.1101/2021.05.25.445613; this version posted May 25, 2021. The copyright holder for this preprint (which was not certified by peer review) is the author/funder. All rights reserved. No reuse allowed without permission.

lead to increased cAMP/PKA, which has been shown to enhance synaptic strength through different aspects, such as by increasing neurite outgrowth[45–47] and modulating different ion channels[48–54]. Intriguingly, one recent study demonstrated that cAMP/PKA induces calcium influx through voltage-gated calcium channel, which pushes the neuronal network towards a large-scale and synchronized burst activity[55]. Consistently, our calcium imaging data showed increased synchronized activity in *SETD1A*$^{+/-}$ networks. This suggests there could be a similar cAMP-triggered mechanism in our model, which contributes to the network phenotype we observe.

cAMP signaling has been implicated in neurodevelopmental and neuropsychiatric disorders, including SCZ[56–61] , bipolar disorder[62, 63], Fragile X syndrome[64–66] and autism[67, 68]. For example, in patients with bipolar disorder, cAMP/PKA signaling is upregulated[63], while in the case of Fragile X syndrome, cAMP/PKA signaling is decreased[64]. These findings emphasize the essential role of balanced cAMP activity in normal brain function, making it an appealing therapeutic target. In our model, acute treatment of antagonists of cAMP/PKA was able to partly rescue the *SETD1A*$^{+/-}$ network phenotype, but not completely. This is within expectation, considering that pharmacological manipulation was performed in the late-stage cultures when the neuronal networks were already fully matured and where the effect of *SETD1A* haploinsufficiency accumulated for longer than 7 weeks. Furthermore, we cannot rule out the possibilities that other downstream effectors of cAMP such as EPAC (a guanine-nucleotide-exchange factor) and cyclic-nucleotide-gated ion channels[69], are also partly involved in the phenotype caused by *SETD1A* haploinsufficiency. In addition, since cAMP/PKA signaling functions in various cells types, therapeutic intervention of its activity therefore needs further clarification of its cell type specific roles. In this context, future studies should comprehensively investigate whether upregulated cAMP/PKA signaling caused by *SETD1A* haploinsufficiency also applies to other brain regions or other cell types related to SCZ or neurodevelopmental disorders, such as serotonergic[70] or dopaminergic neurons[71], as well as glial cells[72]. Although we found evidence for a prominent contribution of glutamatergic neurons to

bioRxiv preprint doi: https://doi.org/10.1101/2021.05.25.445613; this version posted May 25, 2021. The copyright holder for this preprint (which was not certified by peer review) is the author/funder. All rights reserved. No reuse allowed without permission.

the network phenotype in *SETD1A*$^{+/-}$ E/I cultures, there may also be cell-autonomous and non-autonomous effects of SETD1A on GABAergic neurons and GABAergic signaling.

Taken together, our data suggest glutamatergic synaptic dysfunction is a potential pathogenic mechanism of *SETD1A* haploinsufficiency-associated disorders and we identified cAMP/PKA dysregulation as an underlying mechanism responsible for the altered network phenotype in *SETD1A*$^{+/-}$ cultures. Our findings also emphasize the relevance and potential of human neuronal *in vitro* model for unraveling the biology of neurodevelopmental disorders and developing novel therapeutic strategies.

bioRxiv preprint doi: https://doi.org/10.1101/2021.05.25.445613; this version posted May 25, 2021. The copyright holder for this preprint (which was not certified by peer review) is the author/funder. All rights reserved. No reuse allowed without permission.

Materials and Methods

hiPSC culture

hiPSCs used in this study were obtained from reprogrammed fibroblasts[15]. hiPSCs were cultured on a 6-well plate pre-coated with 1:15 (diluted in DMEM/F12 medium) Matrigel (Corning, #356237) in Essential 8 Flex medium (Thermo Fisher Scientific) supplemented with primocin (0.1 g/ml, Invitrogen) at 37°C/5%CO_2. hiPSCs were infected with *Ascl1* or *Ngn2* and *rtTA* lentivirus (The transfer vector used for the rtTA lentivirus is pLVX-EF1α-(Tet-On-Advanced)-IRES-G418(R); The transfer vector used for the Ngn2 lentivirus is pLVX-(TRE-thight)-(MOUSE) Ngn2-PGK-Puromycin(R); The transfer vector used for the Ascl1 lentivirus is pLV[TetOn]-Puro-TRE>mAscl1. All the plasmids are available upon request). Medium was supplemented with puromycin (0.5 g/ml) and G418 (50 g/ml). Medium was refreshed every 2-3 days and hiPSCs were passaged twice per week using an enzyme-free reagent (ReLeSR, Stem Cell Technologies).

Neuronal differentiation

The neuronal differentiation protocol used in this article was previously described[14]. Glutamatergic neurons were either cultured alone or in coculture with GABAergic neurons. When cocultured, GABAergic neurons were plated at days *in vitro* (DIV) 0 and transduced with AAV2-hSyn-mCherry (UNC Vector Core) for visualization. After 4 hours incubation, cultures were washed twice with DMEM/F12 (Thermo Fisher Scientific) after which glutamatergic neurons were plated into the well. hiPSCs were plated in E8 flex supplemented with doxycycline (4 µg/ml), Revitacell (1:100, Thermo Fisher Scientific) and Forskolin (10 µM, Sigma). At DIV 1 cultures were switched to DMEM/F12 containing Forskolin, N2 (1:100, Thermo Fisher Scientific), non-essential amino acids (1:100, Sigma), primocin (0.1 µg/ml, Invivogen), NT3 (10 ng/ml, PromoCell), BDNF (10 ng/ml, PromoCell), and doxycycline (4µg/ml). To support neuronal maturation, freshly prepared rat astrocytes were added to the culture in a 1:1 ratio at DIV 2. At DIV 3 the medium was changed to Neurobasal medium (Thermo

bioRxiv preprint doi: https://doi.org/10.1101/2021.05.25.445613; this version posted May 25, 2021. The copyright holder for this preprint (which was not certified by peer review) is the author/funder. All rights reserved. No reuse allowed without permission.

Fisher Scientific) supplemented with Forskolin (10 µM, Sigma), B-27 (Thermo Fisher Scientific), glutaMAX (Thermo Fisher Scientific), primocin (0.1 µg/ml), NT3 (10 ng/ml), BDNF (10 ng/ml), and doxycycline (4 µg/ml). To remove the proliferating cells from the culture, cytosine-b-D-arabinofuranoside (Ara-C, 2 µM, Sigma) was added to the medium at DIV3. From DIV 6 onwards half of the medium was refreshed three times a week. From DIV 10 onwards, the medium was additionally supplemented with 2.5% FBS (Sigma) to support astrocyte viability. After DIV 13, Forskolin and doxycycline were removed from the medium. Cultures were kept at least until DIV49.

CRISPR/Cas9 editing of *SETD1A*

CRISPR/Cas9 technology was used to create a heterozygous indel mutation in exon 7 of *SETD1A* in a healthy hiPSC line derived from a male, 30 years old[73]. In brief, sgRNAs were designed to specifically target *SETD1A* (GTCCTTGGGGCCAGAGATAC AGG), and then cloned into pSpCas9(BB)-2A-Puro (PX459) V2.0 (Addgene #62988). Single-cell suspension of hiPSCs was nucleofected with 5 µg of the generated SpCas9-sgRNA plasmid using the P3 Primary Cell 4D-Nucleofector Kit (Lonza, #V4XP-3024) in combination with the 4D Nucleofector Unit X (Lonza, #AAF-1002X), program CA-137. After nucleofection, cells were resuspended in E8 Flex supplemented with Revitacell and seeded on Matrigel pre-coated plates. One day after the nucleofection, 0.5 µg puromycin was added for 24 hours. Puromycin-resistant colonies were manually picked and Sanger Sequencing was performed to ensure heterozygous editing of exon 7.

Immunocytochemistry

Cells seeded on coverslips were fixed with 4% paraformaldehyde supplemented with 4% sucrose for 15 min at room temperature, followed by permeabilization with 0.2% triton for 10 min. Nonspecific binding sites were blocked by incubation in 5% normal goat serum for 1 hour at room temperature. Cells were incubated with primary antibodies overnight at 4°C. The second day, secondary antibodies, conjugated to Alexa-fluorochromes, were added and incubated for 1 hour at room temperature.

bioRxiv preprint doi: https://doi.org/10.1101/2021.05.25.445613; this version posted May 25, 2021. The copyright holder for this preprint (which was not certified by peer review) is the author/funder. All rights reserved. No reuse allowed without permission.

Hoechst 33342 was used to stain the nucleus before cells were mounted with fluorescent mounting medium (DAKO, #S3023). The following primary antibodies were used: rabbit anti-MAP2 (1:1000, Abcam, #ab32454); Mouse anti-Gephyrin (1:1000, Synaptic Systems 147011); Rabbit anti-VGAT (1:500, Synaptic systems 131013); Guinea pig anti-Synapsin 1/2 (1:1000, Synaptic Systems 106004); Mouse anti-Homer1 (1:500, Synaptic Systems 160011); Rabbit anti-Phospho-CREB (1:500, Cell Signaling 87G3 9198). Secondary antibodies that were used are: Goat-anti rabbit Alexa 568 (1:1000, Invitrogen, A11036); Goat-anti-mouse Alexa 488 (1:1000, Invitrogen, A11029); Goat anti-guinea pig Alexa Fluor 568 (1:2000, Invitrogen, A11075); Goat anti-guinea pig Alexa Fluor 647 (1:1000, Invitrogen, A21450). Cells were imaged at 63x magnification using the Zeiss Axio Imager Z1 equipped with ApoTome. Fluorescent images were analyzed using FIJI software[74]. Synapse puncta were counted manually and normalized to the length of the dendritic branch where they reside.

Neuron reconstruction

To investigate the morphological effect caused by *SETD1A* haploinsufficiency, neurons were fixed and labeled with MAP2 antibody. To distinguish GABAergic neurons from glutamatergic neurons, we infected GABAergic neurons with AAV2-hSyn-mCherry for (UNC Vector Core) visualization. We chose two time points to fix the neurons: DIV21 and DIV49. DIV21 represents a relatively unmatured state, while DIV49 represents a mature state. This allows us to compare the morphological phenotype at different developmental stages. Fluorescent images of MAP2-labelled neurons were taken at 20x magnification using Zeiss Axio Imager Z1 equipped with ApoTome. The images were stitched using Fiji 2018 software with the stitching plugin and followed by reconstruction using Neurolucida 360 (Version 2017.01.4, Microbrightfield Bioscience). The 3-dimensional reconstructions and quantitative morphometrical analyses focused on the somatodendritic organization of the neurons. The axon was excluded based on its long, thin properties and far-reaching projections. Neurons that had at least two primary dendrites were selected for reconstruction and

bioRxiv preprint doi: https://doi.org/10.1101/2021.05.25.445613; this version posted May 25, 2021. The copyright holder for this preprint (which was not certified by peer review) is the author/funder. All rights reserved. No reuse allowed without permission.

further analysis. For morphometrical analysis, we determined soma size, number of primary dendrites, dendritic nodes and ends and total or mean dendritic length as well as covered surface by dendritic trees. In addition, we also investigated dendritic complexity by performing Sholl analysis. Sholl profile was obtained by applying a series of concentric circles at 20 µm interval from the soma center, subsequently, dendritic length, number of intersections and number of nodes of the neurons were measured for each distance interval.

MEA recordings and analysis

All recordings were performed using the 24-wells MEA system (Multichannel Systems, MCS GmbH, Reutlingen, Germany). MEA devices were composed of 24 independent wells with embedded microelectrodes (i.e., 12 electrodes/well, 80 µm in diameter and spaced 300 µm apart). Recordings and analysis were performed according to previous published protocols[17]. Briefly, spontaneous electrophysiological activity of hiPSC-derived neuronal networks cultured on MEA was recorded for 10 minutes in a recording chamber which was constantly maintained at 37^0C with 95%O_2 and 5%CO_2. Before recording, cultures on MEA were allowed to adapt for 10 minutes in the recording chamber. The recording was sampled at 10 kHz, and filtered with a high-pass filter with a 100 Hz cut-off frequency and a low-pass filter with a 3500 Hz cut-off frequency. The spike detection threshold was set at ± 4.5 standard deviations. Spike, burst and network burst detection was performed by a built-in algorithm in Mulitwell Analzer software (Multichannel Systems), and a custom-made MATLAB (The Mathworks, Natrick) code to extract parameters characterizing network activity. Mean firing rate (MFR) was calculated as the average of the spike frequency of all channels across one MEA well. From the burst detection, the number of bursting channels (above threshold 0.4 burst/s and at least 5 spikes in burst with a minimal inter-burst-interval of 100ms) was determined. A network burst was defined when at least 80% of the channels in one well exhibited a synchronous burst.

Whole cell patch clamp

bioRxiv preprint doi: https://doi.org/10.1101/2021.05.25.445613; this version posted May 25, 2021. The copyright holder for this preprint (which was not certified by peer review) is the author/funder. All rights reserved. No reuse allowed without permission.

Coverslips were placed in the recording chamber of the electrophysiological setup, continuously perfused with oxygenated (95% O2/ 5% CO2) ACSF at 32°C containing (in mM) 124 NaCl, 1.25 NaH2PO4, 3 KCl, 26 NaHCO3, 11 Glucose, 2 CaCl2, 1 MgCl2. Patch pipettes with filament (ID 0.86mm, OD1.05mm, resistance 6-8 MΩ) were pulled from borosilicate glass (Science Products GmbH, Hofheim, Germany) using a Narishige PC-10 micropipette puller (Narishige, London, UK). For all recordings of intrinsic properties and spontaneous activity and mPSC activity, a potassium-based intracellular solution containing (in mM) 130 K-Gluconate, 5 KCl, 10 HEPES, 2.5 MgCl2, 4 Na2-ATP, 0.4 Na3-ATP, 10 Na-phosphocreatine and 0.6 EGTA was used, with a pH of 7.2 and osmolality of 290 mOsmol/L. Resting membrane potential (Vrmp) was measured immediately after generation of a whole-cell configuration. Further analysis of active and passive membrane properties was cwonducted at a holding potential of -60 mV. Passive membrane properties were determined via voltage steps of -10 mV. Active intrinsic properties were measured with a stepwise current injection protocol. Spontaneous activity and mPSCs were measured by 10 minutes continuous recording at a holding potential of -60mV. For the recording of mPSCs, 1µM TTX was added to the recording medium. Recordings were conducted at either DIV21 and DIV49 (intrinsic properties and sPSCs) or only DIV49 (mPSCs). Cells were visualized with an Olympus BX51WI upright microscope (Olympus Life Science, PA, USA), equipped with a DAGE-MTI IR-1000E (DAGE-MTI, IN, USA) camera) and a CoolLED PE-200 LED system (Scientifica, Sussex, UK) which aided in fluorescent identification of GABAergic neurons. A Digidata 1440A digitizer and a Multiclamp 700B amplifier (Molecular Devices) were used for data acquisition. Sampling rate was set at 20 kHz (intrinsic properties) or 10kHz (sPSCs and mPSCs) and a lowpass 1 kHz filter was used during recording. Recordings were not corrected for liquid junction potential (± 10 mV). Recordings were discarded if series resistance reached >25 MΩ or dropped below a 10:0 ratio of membrane resistance to series resistance. Intrinsic electrophysiological properties were analysed using Clampfit 11.2 (molecular devices, CA, USA), and sPSCs were analysed using MiniAnalysis 6.0.2 (Synaptosoft Inc, GA, USA) as previously described[14]. Regarding

bioRxiv preprint doi: https://doi.org/10.1101/2021.05.25.445613; this version posted May 25, 2021. The copyright holder for this preprint (which was not certified by peer review) is the author/funder. All rights reserved. No reuse allowed without permission.

the analysis of the intrinsic properties: In brief, the adaptation ratio was defined as the Δt action potential 8-9/Δt action potential 2-3. The afterhyperpolarization time was defined as the time from which the repolarization phase reaches the threshold potential to the time at which the most hyperpolarized potential was reached. Action potential half-time was calculated as the time to reach 50% ΔmV of the action potential to the AHP peak.

RNA extraction and sequencing

Total RNA was extracted from three biological replicates of control and *SETD1A*$^{+/-}$ E/I networks and glutamatergic networks respectively (12 samples in total) using the NucleoSpin RNA isolation kit (Machery Nagel, 740955.250) according to the manufacturer's instructions. RNA yield was quantified with a NanoDrop Spectrophotometer (NanoDrop Technologies, Wilmington, DE, USA) and RNA integrity was assessed with Bioanalyzer 2100 RNA 6000 Nano Kit (Agilent Technologies, Santa Clara, CA, USA). All samples had an RNA Integrity Number (RIN) > 9. Library preparation and paired-end RNA-sequencing were carried out at the Norwegian High-Throughput Sequencing Centre (www.sequencing.uio.no). Briefly, libraries were prepared with the TruSeq Stranded mRNA kit from Illumina which involves Poly-A purification to capture coding as well as several non-coding RNAs. The prepared samples were then sequenced on an Illumina NovaSeq SP platform at an average depth of ~50 million reads per sample using a read length of 100 base pairs and an insert size of 350 base pairs.

RNA-seq data processing

Raw sequencing reads were quality assessed with FastQC (Babraham Institute). To pass the initial QC check, the average Phred score of each base position across all reads had to be at least 30. Reads were further processed by cutting individual low-quality bases and removing adapter and other Illumina-specific sequences with Trimmomatic V0.32 using default parameters[75]. The trimming process may result in some reads being discarded and their mates thereby unpaired, therefore only reads

bioRxiv preprint doi: https://doi.org/10.1101/2021.05.25.445613; this version posted May 25, 2021. The copyright holder for this preprint (which was not certified by peer review) is the author/funder. All rights reserved. No reuse allowed without permission.

that remained paired after trimming were used for downstream analyses. Since the cultures contained both hiPSC-derived neurons as well as rat astrocytes which were added to support neuronal maturation, sequencing reads were separated according to their species of origin using the *in silico* RNA-seq read sorting tool Sargasso[76], which was able to successfully eliminate sequencing reads stemming from rat astrocytes (**Figure S11**). To quantify gene expression levels, reads mapped by Sargasso were summarized at the gene level using featureCounts[77] guided by ENSEMBL annotations.

Differential expression (DE) analysis and over-representation test

To evaluate the species separation performance of Sargasso, bioinformatical estimation of cell type abundances (deconvolution) was carried out with CIBERSORTx[78] using expression signatures for human neurons and rodent astrocytes[79] (**Figure S11**). Before conducting the DE analyses, genes with very low to zero expression were removed by filtering out any gene with ≤1 counts per million (CPM) in 3 or more samples (the smallest group size). DE analysis was performed using the statistical R package DESeq2[80], which provides methods to test for differentially expressed genes by use of negative binomial generalized models. The DESeq2 workflow begins by taking raw read count data as input and applies an internal normalization method that corrects for sequencing depth and RNA composition. The standard DE analysis consists of size factor estimation, dispersion estimation, and model fitting, as well as an independent filtering step that optimizes the number of significant DE genes. After the pre-filtering and independent filtering steps, a total of 14,144 genes were retained and examined in the DE analyses. A DE gene was considered significant if the FDR was <0.05. Gene Ontology (GO) enrichment tests of significant DE gene sets were conducted with the over-representation analysis tool clusterProfile[81] using the enrichGO function. A GO term was considered significantly enriched if the FDR was <0.05. Disease association analysis was performed with the R package disgenet2r[18] using both the CURATED database, which includes more than 10,000 somatic and mental disorders, and the

bioRxiv preprint doi: https://doi.org/10.1101/2021.05.25.445613; this version posted May 25, 2021. The copyright holder for this preprint (which was not certified by peer review) is the author/funder. All rights reserved. No reuse allowed without permission.

PSYGENET, which includes 109 mental diseases. In both cases, FDR<0.05 was used as the threshold to determine significant disease association.

Chemicals

All reagents were prepared fresh into concentrated stocks, and stored frozen at −20 °C. The following compounds were used in pharmacological experiments: Picrotoxin (100 mM in DMSO, Tocris 1128); Forskolin (12 mM in DMSO, Sigma F6886); SQ22536 (50 mM in DMSO, Sigma S153); H89 (5 mM in MQ, Tocris 2910); KT5720 (1 mM in DMSO, Tocris 1283). For all experiment on MEA, before adding chemical to the cultures, an aliquot of the concentrated stock was first diluted in DPBS at room temperature. Then, the appropriate amount of working dilution was added directly to wells on the MEA and mixing was primarily through diffusion into the (500 µl) cell culture medium.

Pharmacological experiment

Control and *SETD1A*$^{+/-}$ networks on MEA were treated with Picrotoxin (PTX, 100 µM), Forskolin (1 µM), H89 (2 µM) and KT5720 (1 µM) at DIV49 or DIV51, and SQ22536 (100 µM) at DIV42 after a 20 min recording of spontaneous activity. Then the recording was stopped temporarily, and the compounds were added to the MEA. We recorded neuronal network activity for 10 min after 5 min treatment of PTX, 60 min treatment of Forskolin, KT5720, H89 and 8 days treatment of SQ22536.

Quantitative polymerase chain reaction

RNA samples were isolated from cells using the NucleoSpin RNA isolation kit (Machery Nagel, 740955.250) according to the manufactures' instructions. cDNAs were synthesized by iScript cDNA synthesis kit (BioRad, 1708891) and cleaned up using the Nucleospin Gel and PCR clean-up kit (Machery Nagel, 740609.250). PCR reactions were performed in the 7500 Fast Real Time PCR System apparatus (Applied Biosystems) by using GoTaq qPCR master mix 2x with SYBR Green (Promega, A600A) according to the manufacturer's protocol. Reverse

bioRxiv preprint doi: https://doi.org/10.1101/2021.05.25.445613; this version posted May 25, 2021. The copyright holder for this preprint (which was not certified by peer review) is the author/funder. All rights reserved. No reuse allowed without permission.

transcriptase-negative controls and no template-controls were included in each experiment. The arithmetic mean of the C_t values of the technical replicates was used for calculations. Relative mRNA expression levels for all genes of interest were calculated using the $2^{\wedge-\Delta\Delta Ct}$ method with standardization to GAPDH expression level. All expression analyses were done for at least three different biological replicates.

Western Blot

For Western blot, cell lysates were made from hiPSC cultures that were 80-90% confluent well on a 6-well plate. Medium was always refreshed the day before. To lyse the cells, medium was removed and the well was washed with 2 ml ice cold PBS before 100 µl lysis buffer were applied (RIPA buffer supplemented with PhosSTOP; Roche) and protease inhibitors (complete Mini, EDTA free; Roche). Before blotting the protein, concentration was determined by means of a Pierce™ BCA protein assay (Thermo Scientific 23225). For each sample, the same amount of protein around 15 µg was loaded and separated by SDS-PAGE. Depending on the primary antibody, separated proteins were transferred to PVDF membrane (BioRad). Primary antibodies were used are: Mouse anti-SET1A (1: 500, Santa Cruz 515590); Mouse anti-γ-tubulin (1:1000, Sigma T5326). For visualization horseradish peroxidase-conjugated secondary antibodies were used: Goat anti-mouse (1:20000; Jackson Immuno Research Laboratories 115-035-062).

Calcium imaging

For calcium imaging, cultures were incubated with 4 µg/ml Fluo-8-AM for 30 min at 37°C. After incubation, we removed the excess dye by washing the cells 3 times with HHBS. The cells were then left in culture medium to recover for 15 min. To image the cells, we placed them under the microscope (SliceScope Pro 2000, Scientifica). We continuously perfused the recording chamber with oxygenated (95% O_2/ 5% CO_2) and artificial cerebrospinal fluid (ACSF) that was composed of (in mM) 124 NaCl, 3 KCl, 1.25 NaH_2PO_4, 2 $CaCl_2$, 1 $MgCl_2$, 26 $NaHCO_3$, 10 Glucose and heated to 37°C. Imaging was performed using a sCMOS camera (Prime BSI Express, Teledyne

bioRxiv preprint doi: https://doi.org/10.1101/2021.05.25.445613; this version posted May 25, 2021. The copyright holder for this preprint (which was not certified by peer review) is the author/funder. All rights reserved. No reuse allowed without permission.

Photometrics) controlled by Micro-Manager acquisition software (NIH). Fluo-8-AM in the cells was excited at 470 nm by LED (KSL470, Rapp OptoElectronic). We recorded the cells for 2 min with frame rate of 10 Hz. After recording, we analysed the video using Matlab (The Math Works, Inc. MATLAB. Version 2020b) with a home-made script based on Sun et al[82]. Circular ROIs were chosen by hand at the centre of the soma with a diameter of 10 µm. We obtained the fluorescent change over time which is defined as $\Delta F/F = (F-F_0)/F_0$. Furthermore, the decay of baseline intensity due to bleaching was corrected by exponential fitting to the baseline. Additionally, the traces of each location were analysed for a synchronous firing rate among the selected ROIs to determine network patterns.

Data analysis

The statistical analysis of the data were performed using GraphPad Prism 8 (GraphPad Software, Inc., CA, USA). We ensured normal distribution using a Shapiro-Wilk normality test. Analysis was done using unpaired Student's t tests when comparing two variables at a single time point, or one-way ANOVA with sequential post hoc Bonferroni corrections. Results with p values lower than 0.05 were considered as significantly different. $p < 0.05$ (*), $p < 0.01$ (**), $p < 0.001$ (***). Data is shown as mean ± standard error of the mean (SEM). Details of the statistical tests used for the different analyses are reported in the respective figure legends.

Acknowledgements

This work was supported by grants from: ERA-NET NEURON-102 SYNSCHIZ grant (NWO) 013-17-003 4538 (to D.S) and ERA-NET NEURON DECODE! grant (NWO) 013.18.001 (to N.N.K); The Netherlands Organization for Scientific Research, NWO-CAS grant 012.200.001 (to N.N.K); the Netherlands Organization for Health Research and Development ZonMw grant 91217055 (to. H.v.B and N.N.K); SFARI grant 610264 (to N.N.K); Marie Curie Actions European Fellowship 794273 (to N.K);

bioRxiv preprint doi: https://doi.org/10.1101/2021.05.25.445613; this version posted May 25, 2021. The copyright holder for this preprint (which was not certified by peer review) is the author/funder. All rights reserved. No reuse allowed without permission.

South-Eastern Norway Regional Health Authority #2018094 (to S.D); China scholarship council 201806210076 (to S.W).

Author contribution

S.W, D.S and N.N.K conceived and designed all the experiments. D.S, N.N.K and H.v.B supervised the study. S.W, J.v.R, I.A, N.K, N.M, A.B, E.L, K.W, C.S performed all experiments. S.W, J.v.R, I.A, N.K, N.M, A.B, D.S, N.N.K performed data analysis. S.W, D.S, J.v.R, I.A and N.N.K wrote the manuscript. H.v.B, S.D and T.K edited the manuscript.

Competing interests

The authors declare no competing interests.

bioRxiv preprint doi: https://doi.org/10.1101/2021.05.25.445613; this version posted May 25, 2021. The copyright holder for this preprint (which was not certified by peer review) is the author/funder. All rights reserved. No reuse allowed without permission.

Reference

1. Skene NG, Bryois J, Bakken TE, Breen G, Crowley JJ, Gaspar HA, et al. Genetic identification of brain cell types underlying schizophrenia. Nat Genet. 2018;50:825–833.
2. Legge SE, Santoro ML, Periyasamy S, Okewole A, Arsalan A, Kowalec K. Genetic architecture of schizophrenia: a review of major advancements. Psychol Med. 2021:1–10.
3. Hilker R, Helenius D, Fagerlund B, Skytthe A, Christensen K, Werge TM, et al. Heritability of Schizophrenia and Schizophrenia Spectrum Based on the Nationwide Danish Twin Register. Biol Psychiatry. 2018;83:492–498.
4. Legge SE, Santoro ML, Periyasamy S, Okewole A, Arsalan A, Kowalec K. Genetic architecture of schizophrenia: a review of major advancements. Psychol Med. 2021:1–10.
5. Takata A, Xu B, Ionita-Laza I, Roos JL, Gogos JA, Karayiorgou M. Loss-of-Function Variants in Schizophrenia Risk and SETD1A as a Candidate Susceptibility Gene. Neuron. 2014;82:773–780.
6. Singh T, Kurki MI, Curtis D, Purcell SM, Crooks L, McRae J, et al. Rare loss-of-function variants in SETD1A are associated with schizophrenia and developmental disorders. Nat Neurosci. 2016;19:571–577.
7. Singh T, Neale BM, Daly MJ. Exome sequencing identifies rare coding variants in 10 genes which confer substantial risk for schizophrenia on behalf of the Schizophrenia Exome Meta-Analysis (SCHEMA) Consortium*. MedRxiv. 2020:2020.09.18.20192815.
8. Eising E, Carrion-Castillo A, Vino A, Strand EA, Jakielski KJ, Scerri TS, et al. A set of regulatory genes co-expressed in embryonic human brain is implicated in disrupted speech development. Mol Psychiatry. 2019;24:1065–1078.
9. Yu X, Yang L, Li J, Li W, Li D, Wang R, et al. De Novo and Inherited SETD1A Variants in Early-onset Epilepsy. Neurosci Bull. 2019;35:1045–1057.

bioRxiv preprint doi: https://doi.org/10.1101/2021.05.25.445613; this version posted May 25, 2021. The copyright holder for this preprint (which was not certified by peer review) is the author/funder. All rights reserved. No reuse allowed without permission.

10. Kummeling J, Stremmelaar DE, Raun N, Reijnders MRF, Willemsen MH, Ruiterkamp-Versteeg M, et al. Characterization of SETD1A haploinsufficiency in humans and Drosophila defines a novel neurodevelopmental syndrome. Mol Psychiatry. 2020:1–12.

11. Mukai J, Cannavò E, Crabtree GW, Sun Z, Diamantopoulou A, Thakur P, et al. Recapitulation and Reversal of Schizophrenia-Related Phenotypes in Setd1a-Deficient Mice. Neuron. 2019;104:471-487.e12.

12. Nagahama K, Sakoori K, Watanabe T, Kishi Y, Kawaji K, Koebis M. Article Setd1a Insufficiency in Mice Attenuates Excitatory Synaptic Function and Recapitulates Schizophrenia- Related Behavioral Abnormalities ll Setd1a Insufficiency in Mice Attenuates Excitatory Synaptic Function and Recapitulates Schizophrenia-Related . CellReports. 2020;32:108126.

13. Hamm JP, Shymkiv Y, Mukai J, Gogos JA, Yuste R. Aberrant Cortical Ensembles and Schizophrenia-like Sensory Phenotypes in Setd1a+/− Mice. Biol Psychiatry. 2020;88:215–223.

14. Mossink B, van Rhijn J-R, Wang S, Linda K, Vitale MR, Zöller JEM, et al. Cadherin-13 is a critical regulator of GABAergic modulation in human stem-cell-derived neuronal networks. Mol Psychiatry. 2021:1–18.

15. Miyaoka Y, Chan AH, Judge LM, Yoo J, Huang M, Nguyen TD, et al. Isolation of single-base genome-edited human iPS cells without antibiotic selection. Nat Methods. 2014;11:291–293.

16. Owen MJ, Sawa A, Mortensen PB. Schizophrenia. Lancet. 2016;388:86–97.

17. Frega M, Linda K, Keller JM, Gümüş-Akay G, Mossink B, van Rhijn JR, et al. Neuronal network dysfunction in a model for Kleefstra syndrome mediated by enhanced NMDAR signaling. Nat Commun. 2019;10:1–15.

18. Piñero J, Ramírez-Anguita JM, Saüch-Pitarch J, Ronzano F, Centeno E, Sanz F, et al. The DisGeNET knowledge platform for disease genomics: 2019 update. Nucleic Acids Res. 2020;48:D845–D855.

19. Szklarczyk D, Gable AL, Nastou KC, Lyon D, Kirsch R, Pyysalo S, et al. The STRING database in 2021: Customizable protein-protein networks, and

bioRxiv preprint doi: https://doi.org/10.1101/2021.05.25.445613; this version posted May 25, 2021. The copyright holder for this preprint (which was not certified by peer review) is the author/funder. All rights reserved. No reuse allowed without permission.

functional characterization of user-uploaded gene/measurement sets. Nucleic Acids Res. 2021;49:D605–D612.

20. Yim YS, Kwon Y, Nam J, Yoon HI, Lee K, Kim DG, et al. Slitrks control excitatory and inhibitory synapse formation with LAR receptor protein tyrosine phosphatases. Proc Natl Acad Sci U S A. 2013;110:4057–4062.
21. Carroll LS, Owen MJ. Genetic overlap between autism, schizophrenia and bipolar disorder. Genome Med. 2009;1:102.
22. Wang H, Storm DR. Calmodulin-regulated adenylyl cyclases: Cross-talk and plasticity in the central nervous system. Mol Pharmacol. 2003;63:463–468.
23. Qiu L, LeBel RP, Storm DR, Chen X. Type 3 adenylyl cyclase: A key enzyme mediating the cAMP signaling in neuronal cilia. Int J Physiol Pathophysiol Pharmacol. 2016;8:95–108.
24. Pieroni JP, Harry A, Chen J, Jacobowitz O, Magnusson RP, Iyengar R. Distinct characteristics of the basal activities of adenylyl cyclases 2 and 6. J Biol Chem. 1995;270:21368–21373.
25. Evripioti AA, Ortega-Prieto AM, Skelton JK, Bazot Q, Dorner M. Phosphodiesterase-induced cAMP degradation restricts hepatitis B virus infection. Philos Trans R Soc B Biol Sci. 2019;374.
26. Epstein PM. Different phosphodiesterases (PDEs) regulate distinct phosphoproteomes during cAMP signaling. Proc Natl Acad Sci U S A. 2017;114:7741–7743.
27. Keravis T, Lugnier C. Cyclic nucleotide phosphodiesterase (PDE) isozymes as targets of the intracellular signalling network: Benefits of PDE inhibitors in various diseases and perspectives for future therapeutic developments. Br J Pharmacol. 2012;165:1288–1305.
28. Tasken Y, Skhlhegghl S, Solberg$ R, Anderssonll KB, Taylor SS, Lean T, et al. THE JOURNAL OF BIOLOGICAL CHEMISTRY Novel Isozymes of cAMP-dependent Protein Kinase Exist in Human Cells Due to Formation of RIa-RIP Heterodimeric Complexes*. vol. 268. 1993.

bioRxiv preprint doi: https://doi.org/10.1101/2021.05.25.445613; this version posted May 25, 2021. The copyright holder for this preprint (which was not certified by peer review) is the author/funder. All rights reserved. No reuse allowed without permission.

29. Delghandi MP, Johannessen M, Moens U. The cAMP signalling pathway activates CREB through PKA, p38 and MSK1 in NIH 3T3 cells. Cell Signal. 2005;17:1343–1351.

30. Namkoong S, Kim CK, Cho YL, Kim JH, Lee H, Ha KS, et al. Forskolin increases angiogenesis through the coordinated cross-talk of PKA-dependent VEGF expression and Epac-mediated PI3K/Akt/eNOS signaling. Cell Signal. 2009;21:906–915.

31. Schiller M, Dennler S, Anderegg U, Kokot A, Simon JC, Luger TA, et al. Increased cAMP levels modulate transforming growth factor-β/smad-induced expression of extracellular matrix components and other key fibroblast effector functions. J Biol Chem. 2010;285:409–421.

32. Song J, Cheon SY, Lee WT, Park KA, Lee JE. PKA Inhibitor H89 (N-[2-p-bromocinnamylamino-ethyl]-5-isoquinolinesulfonamide) Attenuates Synaptic Dysfunction and Neuronal Cell Death following Ischemic Injury. Neural Plast. 2015;2015.

33. Murray AJ. Pharmacological PKA inhibition: All may not be what it seems. Sci Signal. 2008;1:re4–re4.

34. Khazipov R, Luhmann HJ. Early patterns of electrical activity in the developing cerebral cortex of humans and rodents. Trends Neurosci. 2006;29:414–418.

35. Buzsáki G, Draguhn A. Neuronal olscillations in cortical networks. Science (80-). 2004;304:1926–1929.

36. Ford JM, Krystal JH, Mathalon DH. Neural Synchrony in Schizophrenia: From Networks to New Treatments. Schizophr Bull. 2007;33:848–852.

37. Uhlhaas PJ, Singer W. Abnormal neural oscillations and synchrony in schizophrenia. Nat Rev Neurosci. 2010;11:100–113.

38. Spencer KM, Niznikiewicz MA, Nestor PG, Shenton ME, McCarley RW. Left auditory cortex gamma synchronization and auditory hallucination symptoms in schizophrenia. BMC Neurosci. 2009;10:85.

bioRxiv preprint doi: https://doi.org/10.1101/2021.05.25.445613; this version posted May 25, 2021. The copyright holder for this preprint (which was not certified by peer review) is the author/funder. All rights reserved. No reuse allowed without permission.

39. Lee SH, Wynn JK, Green MF, Kim H, Lee KJ, Nam M, et al. Quantitative EEG and low resolution electromagnetic tomography (LORETA) imaging of patients with persistent auditory hallucinations. Schizophr Res. 2006;83:111–119.

40. Lee KH, Williams L, Haig A, Gordon E. “Gamma (40 Hz) phase synchronicity” and symptom dimensions in schizophrenia. Cogn Neuropsychiatry. 2003;8:57–71.

41. Utami KH, Skotte NH, Colaço AR, Binte Mohammad Yusof NA, Sim B, Yeo XY, et al. Integrative analysis identifies key molecular signatures underlying neurodevelopmental deficits in fragile X syndrome. Biol Psychiatry. 2020. 2020. https://doi.org/10.1016/j.biopsych.2020.05.005.

42. Piton A, Gauthier J, Hamdan FF, Lafrenière RG, Yang Y, Henrion E, et al. Systematic resequencing of X-chromosome synaptic genes in autism spectrum disorder and schizophrenia. Mol Psychiatry. 2011;16:867–880.

43. Kang H, Han K, Won SY, Kim HM, Lee YH, Ko J, et al. Slitrk missense mutations associated with neuropsychiatric disorders distinctively impair slitrk trafficking and synapse formation. Front Mol Neurosci. 2016;9:104.

44. Suresh J, Radojicic M, Pesce LL, Bhansali A, Wang J, Tryba AK, et al. Network burst activity in hippocampal neuronal cultures: The role of synaptic and intrinsic currents. J Neurophysiol. 2016;115:3073–3089.

45. Aglah C, Gordon T, Posse de Chaves EI. cAMP promotes neurite outgrowth and extension through protein kinase A but independently of Erk activation in cultured rat motoneurons. Neuropharmacology. 2008;55:8–17.

46. Chu MS, Chang CF, Yang CC, Bau YC, Ho LLT, Hung SC. Signalling pathway in the induction of neurite outgrowth in human mesenchymal stem cells. Cell Signal. 2006;18:519–530.

47. Wan G, Zhou L, Lim QE, Wong YH, Too HP. Cyclic AMP signalling through PKA but not Epac is essential for neurturin-induced biphasic ERK1/2 activation and neurite outgrowths through GFRα2 isoforms. Cell Signal. 2011;23:1727–1737.

bioRxiv preprint doi: https://doi.org/10.1101/2021.05.25.445613; this version posted May 25, 2021. The copyright holder for this preprint (which was not certified by peer review) is the author/funder. All rights reserved. No reuse allowed without permission.

48. Gutierrez-Castellanos N, Da Silva-Matos CM, Zhou K, Canto CB, Renner MC, Koene LMC, et al. Motor Learning Requires Purkinje Cell Synaptic Potentiation through Activation of AMPA-Receptor Subunit GluA3. Neuron. 2017;93:409–424.

49. Renner MC, Albers EH, Gutierrez-Castellanos N, Reinders NR, van Huijstee AN, Xiong H, et al. Synaptic plasticity through activation of GluA3-containing AMPA-receptors. Elife. 2017;6.

50. Hell' JW, Yokoyama2 CT, Breeze LJ, Chavkin C, Catterall' WA. Phosphorylation of presynaptic and postsynaptic calcium channels by cAMP-dependent protein kinase in hippocampal neurons. vol. 14. 1995.

51. van der Horst J, Greenwood IA, Jepps TA. Cyclic AMP-Dependent Regulation of Kv7 Voltage-Gated Potassium Channels. Front Physiol. 2020;11.

52. Anderson AE, Adams JP, Qian Y, Cook RG, Pfaffinger PJ, Sweatt JD. Kv4.2 Phosphorylation by cyclic AMP-dependent protein kinase. J Biol Chem. 2000;275:5337–5346.

53. Connors EC, Ballif BA, Morielli AD. Homeostatic regulation of Kv1.2 potassium channel trafficking by cyclic AMP. J Biol Chem. 2008;283:3445–3453.

54. Beaumont V, Zucker RS. Enhancement of synaptic transmission by cyclic AMP modulation of presynaptic I(h) channels. Nat Neurosci. 2000;3:133–141.

55. Thornquist SC, Pitsch MJ, Auth CS, Crickmore MA. Biochemical evidence accumulates across neurons to drive a network-level eruption. Mol Cell. 2021;81:675-690.e8.

56. Millar JK, Pickard BS, Mackie S, James R, Christie S, Buchanan SR, et al. Genetics: DISC1 and PDE4B are interacting genetic factors in schizoprenia that regulate cAMP signaling. Science (80-). 2005;310:1187–1191.

57. Turetsky BI, Moberg PJ. An odor-specific threshold deficit implicates abnormal intracellular cyclic AMP signaling in schizophrenia. Am J Psychiatry. 2009;166:226–233.

bioRxiv preprint doi: https://doi.org/10.1101/2021.05.25.445613; this version posted May 25, 2021. The copyright holder for this preprint (which was not certified by peer review) is the author/funder. All rights reserved. No reuse allowed without permission.

58. Vacic V, McCarthy S, Malhotra D, Murray F, Chou HH, Peoples A, et al. Duplications of the neuropeptide receptor gene VIPR2 confer significant risk for schizophrenia. Nature. 2011;471:499–503.

59. Muly C. Signal transduction abnormalities in schizophrenia: the cAMP system. Psychopharmacol Bull. 2002;36:92–105.

60. Funk AJ, McCullumsmith RE, Haroutunian V, Meador-Woodruff JH. Abnormal activity of the MAPK- and cAMP-associated signaling pathways in frontal cortical areas in postmortem brain in schizophrenia. Neuropsychopharmacology. 2012;37:896–905.

61. Wang H, Xu J, Lazarovici P, Quirion R, Zheng W. cAMP Response Element-Binding Protein (CREB): A Possible Signaling Molecule Link in the Pathophysiology of Schizophrenia. Front Mol Neurosci. 2018;11:255.

62. Ren X, Rizavi HS, Khan MA, Bhaumik R, Dwivedi Y, Pandey GN. Alteration of cyclic-AMP response element binding protein in the postmortem brain of subjects with bipolar disorder and schizophrenia. J Affect Disord. 2014;152–154:326–333.

63. Chang A, Li PP, Warsh JJ. Altered cAMP-dependent protein kinase subunit immunolabeling in post-mortem brain from patients with bipolar affective disorder. J Neurochem. 2003;84:781–791.

64. Berry-Kravis E, Hicar M, Ciurlionis R. Reduced cyclic AMP production in fragile X syndrome: Cytogenetic and molecular correlations. Pediatr Res. 1995;38:638–643.

65. Berry-Kravis E, Huttenlocher PR. Cyclic AMP metabolism in fragile X syndrome. Ann Neurol. 1992;31:22–26.

66. Kelley DJ, Davidson RJ, Elliott JL, Lahvis GP, Yin JCP, Bhattacharyya A. The Cyclic AMP Cascade Is Altered in the Fragile X Nervous System. PLoS One. 2007;2:e931.

67. Kelley DJ, Bhattacharyya A, Lahvis GP, Yin JCP, Malter J, Davidson RJ. The cyclic AMP phenotype of fragile X and autism. Neurosci Biobehav Rev. 2008;32:1533–1543.

bioRxiv preprint doi: https://doi.org/10.1101/2021.05.25.445613; this version posted May 25, 2021. The copyright holder for this preprint (which was not certified by peer review) is the author/funder. All rights reserved. No reuse allowed without permission.

68. Zamarbide M, Mossa A, Muñoz-Llancao P, Wilkinson MK, Pond HL, Oaks AW, et al. Male-Specific cAMP Signaling in the Hippocampus Controls Spatial Memory Deficits in a Mouse Model of Autism and Intellectual Disability. Biol Psychiatry. 2019;85:760–768.

69. Sassone-Corsi P. The Cyclic AMP pathway. Cold Spring Harb Perspect Biol. 2012;4.

70. Carvajal-Oliveros A, Campusano JM. Studying the Contribution of Serotonin to Neurodevelopmental Disorders. Can This Fly? Front Behav Neurosci. 2021;14:12.

71. Eells J. The Control of Dopamine Neuron Development, Function and Survival: Insights From Transgenic Mice and The Relevance to Human Disease. Curr Med Chem. 2005;10:857–870.

72. Blanco-Suárez E, Caldwell ALM, Allen NJ. Role of astrocyte–synapse interactions in CNS disorders. J Physiol. 2017;595:1903–1916.

73. Mandegar MA, Huebsch N, Frolov EB, Shin E, Truong A, Olvera MP, et al. CRISPR Interference Efficiently Induces Specific and Reversible Gene Silencing in Human iPSCs. Cell Stem Cell. 2016;18:541–553.

74. Schindelin J, Arganda-Carreras I, Frise E, Kaynig V, Longair M, Pietzsch T, et al. Fiji: An open-source platform for biological-image analysis. Nat Methods. 2012;9:676–682.

75. Bolger AM, Lohse M, Usadel B. Trimmomatic: a flexible trimmer for Illumina sequence data. Bioinformatics. 2014;30:2114–2120.

76. Qiu J, Dando O, Baxter PS, Hasel P, Heron S, Simpson TI, et al. Mixed-species RNA-seq for elucidation of non-cell-autonomous control of gene transcription. Nat Protoc. 2018;13:2176–2199.

77. Liao Y, Smyth GK, Shi W. FeatureCounts: An efficient general purpose program for assigning sequence reads to genomic features. Bioinformatics. 2014;30:923–930.

bioRxiv preprint doi: https://doi.org/10.1101/2021.05.25.445613; this version posted May 25, 2021. The copyright holder for this preprint (which was not certified by peer review) is the author/funder. All rights reserved. No reuse allowed without permission.

78. Newman AM, Steen CB, Liu CL, Gentles AJ, Chaudhuri AA, Scherer F, et al. Determining cell type abundance and expression from bulk tissues with digital cytometry. Nat Biotechnol. 2019;37:773–782.

79. Zhang Y, Sloan SA, Clarke LE, Caneda C, Plaza CA, Blumenthal PD, et al. Purification and Characterization of Progenitor and Mature Human Astrocytes Reveals Transcriptional and Functional Differences with Mouse. Neuron. 2016;89:37–53.

80. Love MI, Huber W, Anders S. Moderated estimation of fold change and dispersion for RNA-seq data with DESeq2. Genome Biol. 2014;15:550.

81. Yu G, Wang LG, Han Y, He QY. ClusterProfiler: An R package for comparing biological themes among gene clusters. Omi A J Integr Biol. 2012;16:284–287.

82. Sun Z, Südhof TC. A simple Ca2+-imaging approach to neural network analysis in cultured neurons. BioRxiv. 2020:2020.08.09.243576.

bioRxiv preprint doi: https://doi.org/10.1101/2021.05.25.445613; this version posted May 25, 2021. The copyright holder for this preprint (which was not certified by peer review) is the author/funder. All rights reserved. No reuse allowed without permission.

Main Figures

Figure 1. *SETD1A*$^{+/-}$ neuronal networks exhibit dysregulated functional organization. (a) Generation of *SETD1A* isogenic lines (*SETD1A*$^{+/-}$) using CRISPR/Cas9. **(b-c)** qPCR and Western Blot show reduced mRNA (b) and protein level of SETD1A (c). **(d)** Schematic representation of neuronal differentiation workflow. **(e)** Immunofluorescence staining of GABA (green) and MAP2 (red) at DIV49. Scale bar: 30 µm. **(f-g)** Analysis of neuronal activity using MEA recording. **(f)** Representative raster plots (1 min) of electrophysiological activity exhibited by control and *SETD1A*$^{+/-}$ neuronal networks at different time points during development. **(g)** Quantification of network parameters as indicated. Sample size: control n = 40 MEA wells. *SETD1A*$^{+/-}$ n = 63 MEA wells from 5 independent batches. Representative whole-cell voltage-clamp recordings and quantitative analyses of **(h)** spontaneous postsynaptic currents (sPSCs) and **(i)** correlated synaptic inputs (sPSC bursts) in glutamatergic and GABAergic neurons in control and *SETD1A*$^{+/-}$ E/I cultures at DIV49. Glutamatergic neurons: control (n = 15), *SETD1A*$^{+/-}$ (n = 13); GABAergic neurons: control (n = 15), *SETD1A*$^{+/-}$ (n = 12). **(j)** Representative whole-cell voltage-clamp recordings and quantitative analyses of mPSC activity in glutamatergic and GABAergic neurons. Glutamatergic neurons: control (n = 17), *SETD1A*$^{+/-}$ (n = 16); GABAergic neurons: control (n = 16), *SETD1A*$^{+/-}$ (n = 13). Data represent means ± SEM. *P < 0.05, **P < 0.01, ***P < 0.001, one-way ANOVA test and post hoc Bonferroni correction (b-c, g) or Students' T-test with Bonferroni correction for multiple testing (h-k) or Kolmogorov-Smirnov test (h) for comparing control vs. *SETD1A*$^{+/-}$ cultures.

bioRxiv preprint doi: https://doi.org/10.1101/2021.05.25.445613; this version posted May 25, 2021. The copyright holder for this preprint (which was not certified by peer review) is the author/funder. All rights reserved. No reuse allowed without permission.

Figure 2. *SETD1A*$^{+/-}$ neurons show aberrant somatodendritic morphology. (a-b) Representative somatodendritic reconstructions of glutamatergic (a) or GABAergic (b) neurons and Sholl analysis in control and *SETD1A*$^{+/-}$ neurons at DIV21 (Glutamatergic neurons: n = 20 for control, n = 20 for *SETD1A*$^{+/-}$; GABAergic neurons: n = 18 for control, n = 21 for *SETD1A*$^{+/-}$). **(c-d)** Representative somatodendritic reconstructions of glutamatergic (c) or GABAergic (d) neurons and Sholl analysis in control and *SETD1A*$^{+/-}$ networks at DIV49 (Glutamatergic neurons: n = 22 for control, n = 23 for *SETD1A*$^{+/-}$; GABAergic neurons: n = 20 for control, n = 22 for *SETD1A*$^{+/-}$). **(e-f)** Heatmap showing fold change of all the parameters compared to control in reconstruction for glutamatergic neurons (e) and GABAergic neurons (f) at both DIV21 and DIV49. **(g)** Representative images of immunocytochemistry stained for glutamatergic synapse: Synapsin as a presynaptic marker and Homer1 as a postsynaptic marker, and GABAergic synapse: VGAT as a pre-synaptic marker and Gephyrin as a post synaptic marker. Scale bar = 2 µm **(h)** Quantification of the density of co-localised Synapsin/Homer1 and VGAT/Gephyrin puncta (number per 10 µm). (Synapsin/Homer1: n = 25 for control, n = 21 for *SETD1A*$^{+/-}$ at DIV21, n = 25 for control, n = 26 for *SETD1A*$^{+/-}$ at DIV49; VGAT/Gephyrin: n = 18 for control, n = 21 for *SETD1A*$^{+/-}$ at DIV21, n = 24 for control, n = 23 for *SETD1A*$^{+/-}$ at DIV49.) Data represent means ± SEM. *$p < 0.05$, **$p < 0.01$, ***$p < 0.001$, ****$p < 0.001$, two-way ANOVA with post hoc Bonferroni correction (a-d), unpaired Student's t test (e-f) or one-way ANOVA with post hoc Bonferroni correction (h).

bioRxiv preprint doi: https://doi.org/10.1101/2021.05.25.445613; this version posted May 25, 2021. The copyright holder for this preprint (which was not certified by peer review) is the author/funder. All rights reserved. No reuse allowed without permission.

Figure 3. *SETD1A* haploinsufficiency leads to an altered transcriptomic profile. (**a)** PCA showing tight clustering of 3 replicates for each genotype. **(b)** Volcano plots showing differentially expressed genes (DEGs) between *SETD1A*$^{+/-}$ and control E/I cultures. Relative to control, significantly up or down-regulated genes are shown in red. Top 3 upregulated and downregulated DEGs are labeled. **(c)** Disease terms of DisGeNET database associated with DEGs. **(d)** Gene Ontology (GO) term analysis of DEGs. **(e)** Diagram for dysregulated protein network showing the interactions among several synaptic functions using STRING. **(f)** Heatmap showing the fold change of DEGs compared to control in gene sets related to glutamatergic synapse.

Figure 4. *SETD1A*$^{+/-}$ glutamatergic neuronal cultures recapitulate the *SETD1A*$^{+/-}$ E/I network phenotype (a) Schematic of neuronal differentiation workflow. **(b)** Representative raster plots (1 min) of electrophysiological activity measured by MEA from control and *SETD1A*$^{+/-}$ glutamatergic neuronal networks at different time points during development. **(c)** Quantification of network parameters as indicated at DIV49. Sample size: control n = 35 MEA wells. *SETD1A*$^{+/-}$ n = 37 MEA wells from 4 independent batches. **(d-e)** Representative somatodendritic reconstructions of glutamatergic neurons and Sholl analysis in control and *SETD1A*$^{+/-}$ networks at DIV 49 (n = 38 for control. n = 33 for *SETD1A*$^{+/-}$). Scale bar = 40 µm. **(f)** Heat map showing fold change of all the parameters compared to control for reconstructions of glutamatergic neurons at DIV49. **(g)** Representative voltage-clamp recordings of spontaneous inputs (sPSCs) onto glutamatergic neurons at DIV49 activity and the corresponding quantitative analyses of sPSC frequency **(h)** and amplitude **(i). (j)** Representative voltage-clamp recordings of correlated synaptic inputs (sPSC bursts) in control and *SETD1A*$^{+/-}$ glutamatergic neurons at DIV49 and the corresponding quantitative analyses **(k)**. n = 24/17 for control/*SETD1A*$^{+/-}$ DIV49. Data represent means ± SEM. *$p < 0.05$, **$p < 0.01$, ***$p < 0.001$, two-way ANOVA with post hoc Bonferroni correction (e), unpaired Student's t test (c, f) or Students' T-test with Bonferroni correction for multiple testing (h, i, k).

bioRxiv preprint doi: https://doi.org/10.1101/2021.05.25.445613; this version posted May 25, 2021. The copyright holder for this preprint (which was not certified by peer review) is the author/funder. All rights reserved. No reuse allowed without permission.

Figure 5. *SETD1A* haploinsufficiency leads to activation of cAMP/PKA/CREB pathway. (a) GO terms related to second messenger signaling associated with upregulated differentially expressed genes (DEGs) **(b)** Change of mRNA levels of genes coding for adenylyl cyclase (AC) and phosphodiesterases. **(c)** Schematic of cAMP/PKA/CREB pathway and drug target at different steps. **(d-e)** Representative images showing pCREB expression and quantification of intensity of pCREB for control (n = 105 cells), control + forskolin (n = 30 cells) and *SETD1A*$^{+/-}$ neurons (n = 122 cells from 2 independent batches). Scale bar = 10 µm. **(f-g)** Representative raster plot for 30 sec recorded by MEA and quantification of network burst rate showing the effect of AC agonist forskolin on control networks (sample size: control n=10 wells, control + forskolin n = 12 wells, *SETD1A*$^{+/-}$ n = 28 wells). **(h-i)** Representative raster plot for 30 sec recorded by MEA and quantification of network burst rate showing the effect of AC inhibitor SQ22536 on *SETD1A*$^{+/-}$ E/I cultures (sample size: control n=11 wells, *SETD1A*$^{+/-}$ + SQ22536 n = 12 wells, *SETD1A*$^{+/-}$ n =13 wells). **(j-k)** Representative raster plot for 30 sec recorded by MEA and quantification of network burst rate showing the effect of PKA inhibitor H89 and KT5720 on *SETD1A*$^{+/-}$ E/I cultures (sample size: control n=15 wells, *SETD1A*$^{+/-}$ + H89 n = 18 wells, *SETD1A*$^{+/-}$ + KT5820 n = 18 wells, *SETD1A*$^{+/-}$ n = 22 wells). Data represent means ± SEM. *P <0.05, **P < 0.01, ***P < 0.001, one-way ANOVA test and post-hoc Bonferroni correction.

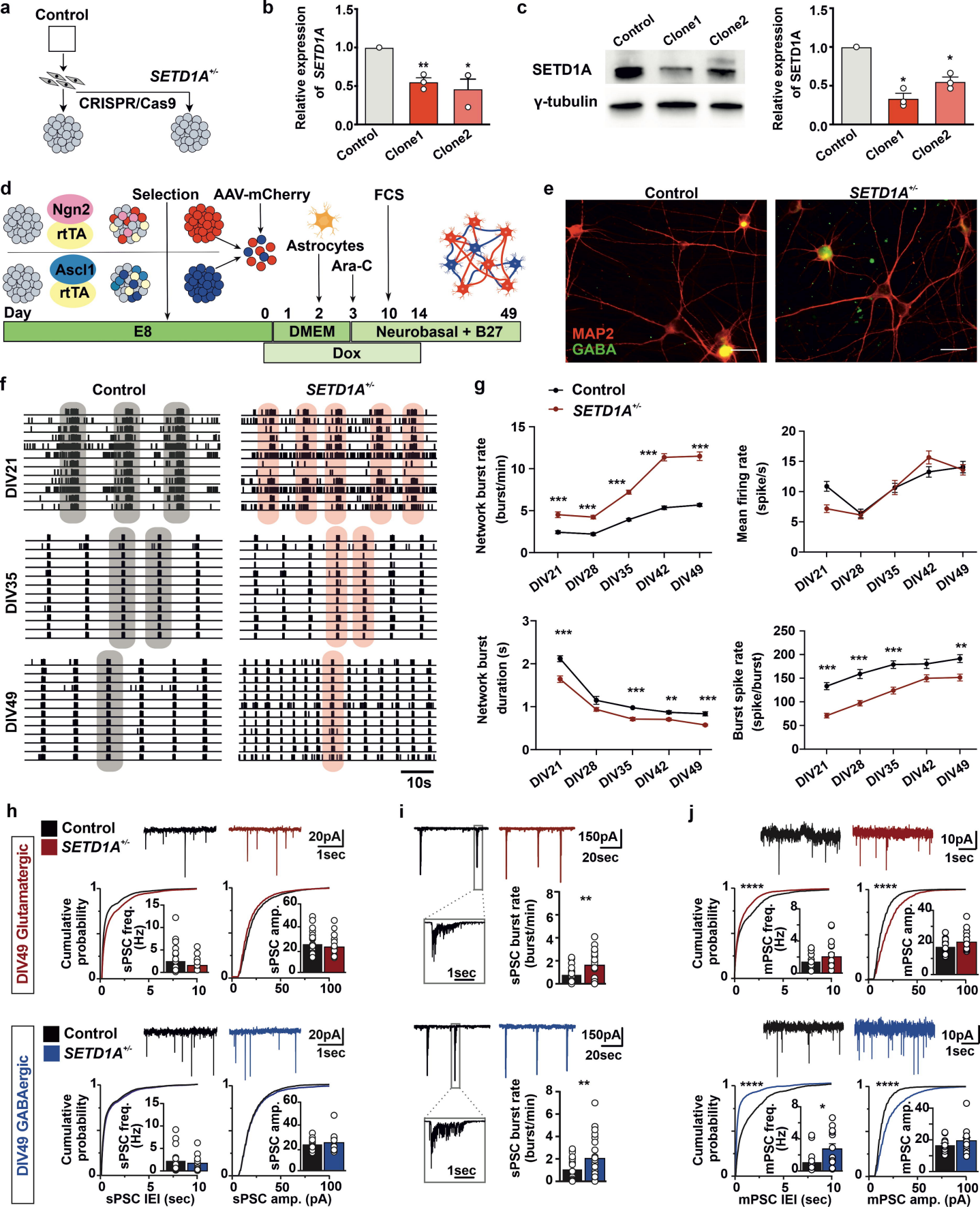
a
Control
SETD1A+/-
CRISPR/Cas9
b
Relative expression of SETD1A
Control
Clone1
Clone2
c
Control
Clone1
Clone2
SETD1A
γ-tubulin
Relative expression of SETD1A
d
Ngn2
rtTA
Ascl1
rtTA
Selection
AAV-mCherry
Astrocytes
Ara-C
FCS
Day
0 1 2 3 10 14 49
E8
DMEM
Neurobasal + B27
Dox
e
Control
SETD1A+/-
MAP2
GABA
f
Control
SETD1A+/-
DIV21
DIV35
DIV49
10s
g
Control
SETD1A+/-
Network burst rate (burst/min)
Mean firing rate (spike/s)
Network burst duration (s)
Burst spike rate (spike/burst)
DIV21
DIV28
DIV35
DIV42
DIV49
h
DIV49 Glutamatergic
Control
SETD1A+/-
20pA
1sec
Cumulative probability
sPSC freq. (Hz)
sPSC amp.
DIV49 GABAergic
sPSC IEI (sec)
sPSC amp. (pA)
i
150pA
20sec
1sec
sPSC burst rate (burst/min)
j
10pA
1sec
mPSC freq. (Hz)
mPSC amp.
mPSC IEI (sec)
mPSC amp. (pA)

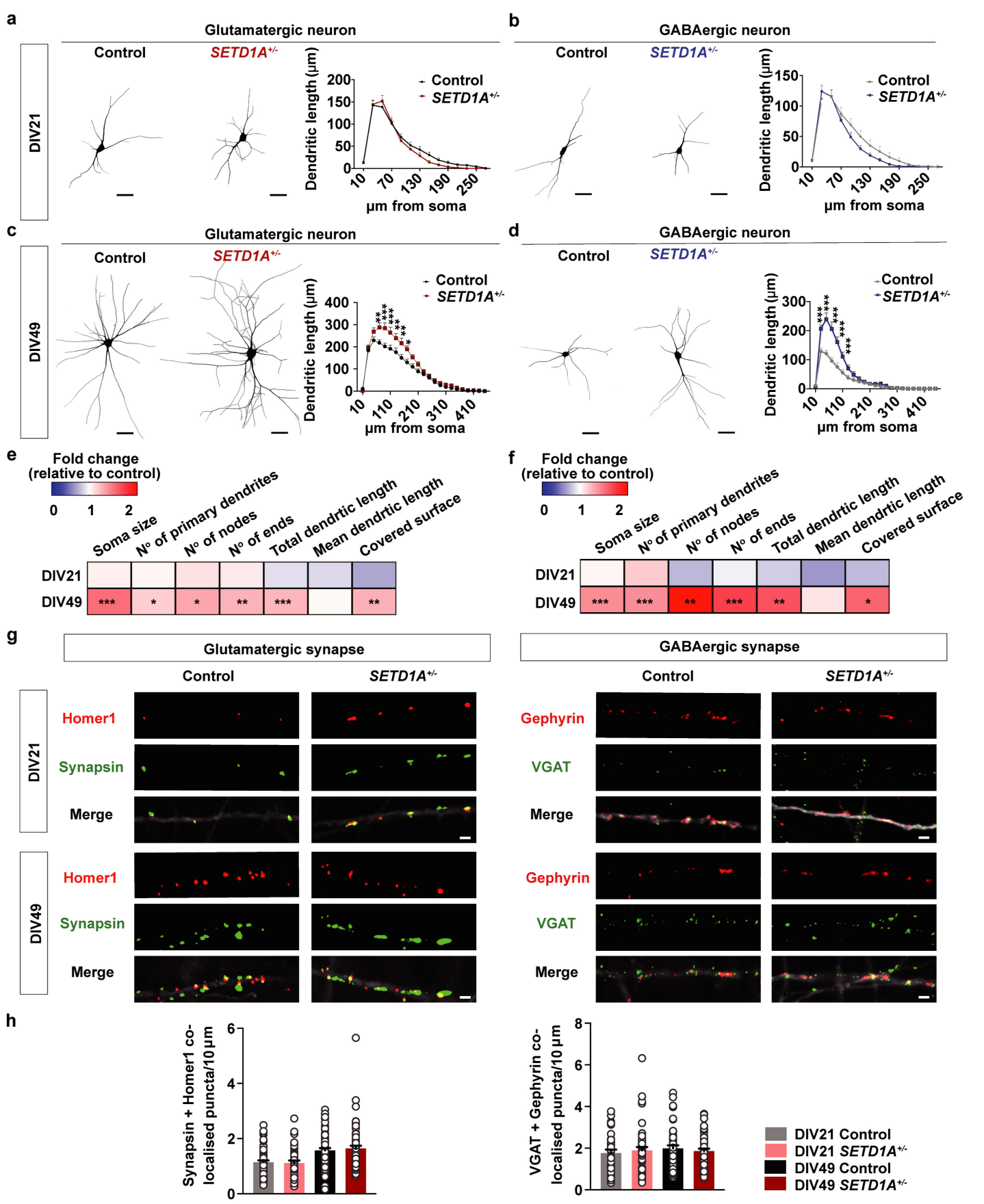
a
Glutamatergic neuron
Control
SETD1A+/-
DIV21
Dendritic length (µm)
Control
SETD1A+/-
µm from soma
b
GABAergic neuron
Control
SETD1A+/-
Dendritic length (µm)
Control
SETD1A+/-
µm from soma
c
Glutamatergic neuron
Control
SETD1A+/-
DIV49
Dendritic length (µm)
Control
SETD1A+/-
µm from soma
d
GABAergic neuron
Control
SETD1A+/-
Dendritic length (µm)
Control
SETD1A+/-
µm from soma
e
Fold change
(relative to control)
0 1 2
Soma size
Nº of primary dendrites
Nº of nodes
Nº of ends
Total dendrtic length
Mean dendrtic length
Covered surface
DIV21
DIV49
f
Fold change
(relative to control)
0 1 2
Soma size
Nº of primary dendrites
Nº of nodes
Nº of ends
Total dendrtic length
Mean dendrtic length
Covered surface
DIV21
DIV49
g
Glutamatergic synapse
Control
SETD1A+/-
DIV21
Homer1
Synapsin
Merge
DIV49
Homer1
Synapsin
Merge
GABAergic synapse
Control
SETD1A+/-
Gephyrin
VGAT
Merge
Gephyrin
VGAT
Merge
h
Synapsin + Homer1 co-localised puncta/10 µm
VGAT + Gephyrin co-localised puncta/10 µm
DIV21 Control
DIV21 SETD1A+/-
DIV49 Control
DIV49 SETD1A+/-

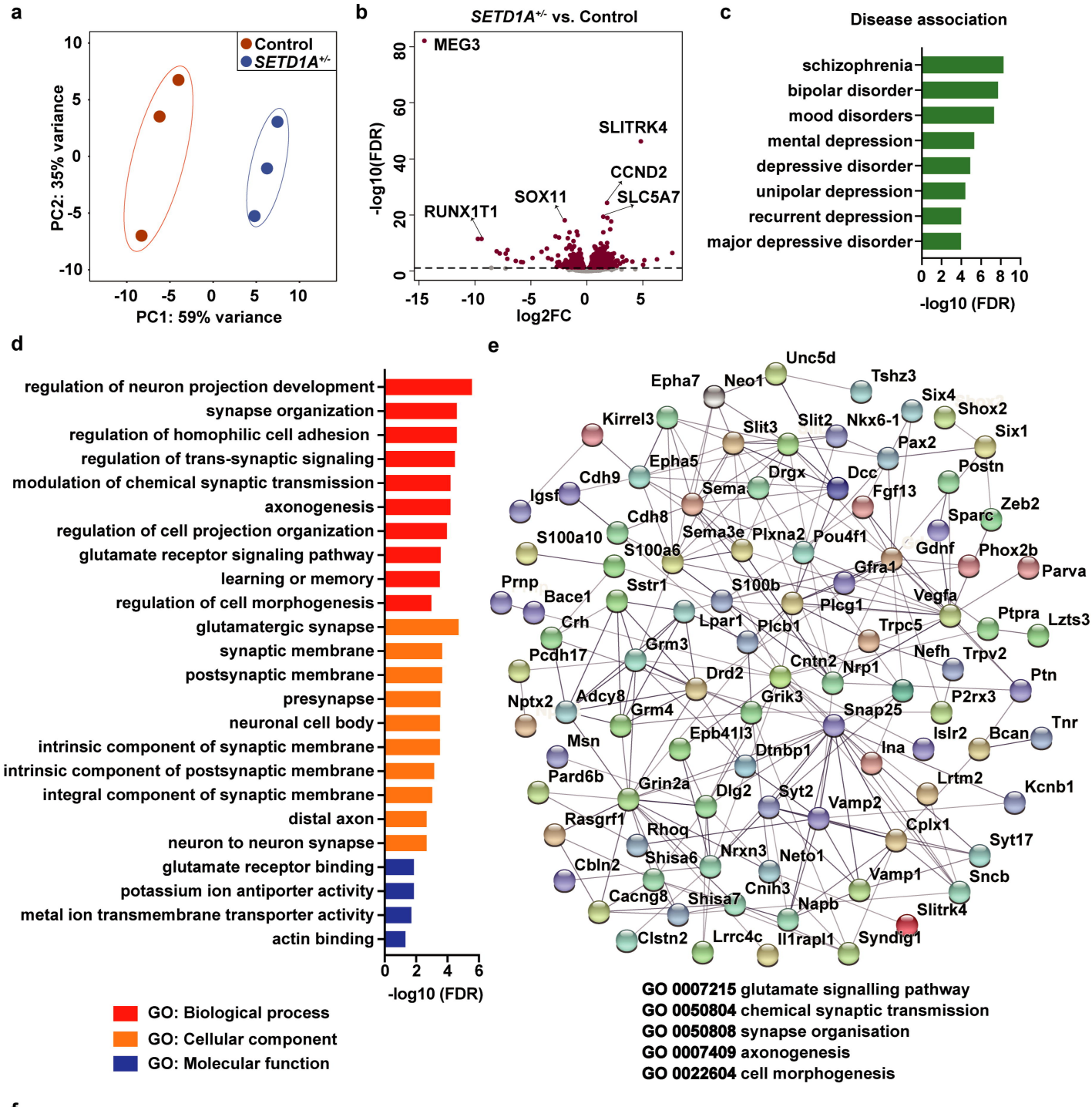
a
Control
SETD1A+/-
PC2: 35% variance
PC1: 59% variance
b
SETD1A+/- vs. Control
MEG3
SLITRK4
CCND2
SLC5A7
SOX11
RUNX1T1
-log10(FDR)
log2FC
c
Disease association
schizophrenia
bipolar disorder
mood disorders
mental depression
depressive disorder
unipolar depression
recurrent depression
major depressive disorder
-log10 (FDR)
d
regulation of neuron projection development
synapse organization
regulation of homophilic cell adhesion
regulation of trans-synaptic signaling
modulation of chemical synaptic transmission
axonogenesis
regulation of cell projection organization
glutamate receptor signaling pathway
learning or memory
regulation of cell morphogenesis
glutamatergic synapse
synaptic membrane
postsynaptic membrane
presynapse
neuronal cell body
intrinsic component of synaptic membrane
intrinsic component of postsynaptic membrane
integral component of synaptic membrane
distal axon
neuron to neuron synapse
glutamate receptor binding
potassium ion antiporter activity
metal ion transmembrane transporter activity
actin binding
-log10 (FDR)
GO: Biological process
GO: Cellular component
GO: Molecular function
e
GO 0007215 glutamate signalling pathway
GO 0050804 chemical synaptic transmission
GO 0050808 synapse organisation
GO 0007409 axonogenesis
GO 0022604 cell morphogenesis
f
GO 0098978: glutamatergic synapse
DTNBP1
NRP1
NPTX2
SPARC
TNR
SNP25
BCAN
VAMP1
CBLN2
LRRC4C
DRD2
CDH8
DLG2
ADCY8
ATP2B2
CLSTN2
ACTC1
CADPS
GRIK3
NETO1
CPLX1
SLTKRK4
PLCB1
GRIN2A
RGS7BP
GRM3
PCDH17
PLCG1
STAU1
HIP1
CHRM3
SYT6
EPH7A
CAMK4
IL1RAPL1
SHISA7
SHISA6
KCND2
Fold change

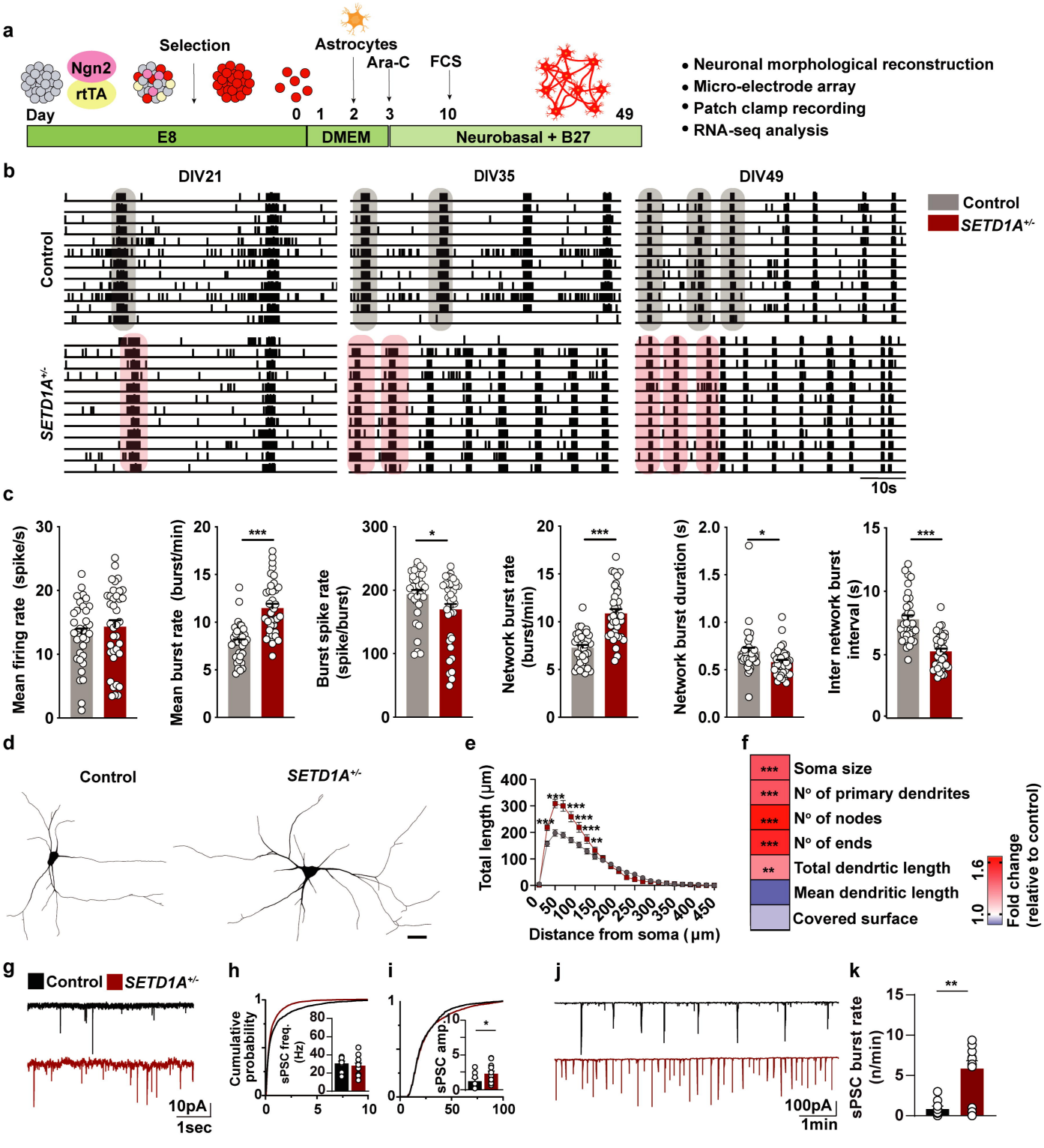
a
Ngn2
rtTA
Selection
Astrocytes
Ara-C
FCS
Day
0 1 2 3 10 49
E8
DMEM
Neurobasal + B27
• Neuronal morphological reconstruction
• Micro-electrode array
• Patch clamp recording
• RNA-seq analysis
b
DIV21
DIV35
DIV49
Control
SETD1A+/-
10s
c
Mean firing rate (spike/s)
Mean burst rate (burst/min)
Burst spike rate (spike/burst)
Network burst rate (burst/min)
Network burst duration (s)
Inter network burst interval (s)
d
Control
SETD1A+/-
e
Total length (µm)
Distance from soma (µm)
f
Soma size
N° of primary dendrites
N° of nodes
N° of ends
Total dendrtic length
Mean dendritic length
Covered surface
Fold change (relative to control)
g
Control
SETD1A+/-
10pA
1sec
h
Cumulative probability
sPSC freq. (Hz)
i
sPSC amp.
j
100pA
1min
k
sPSC burst rate (n/min)

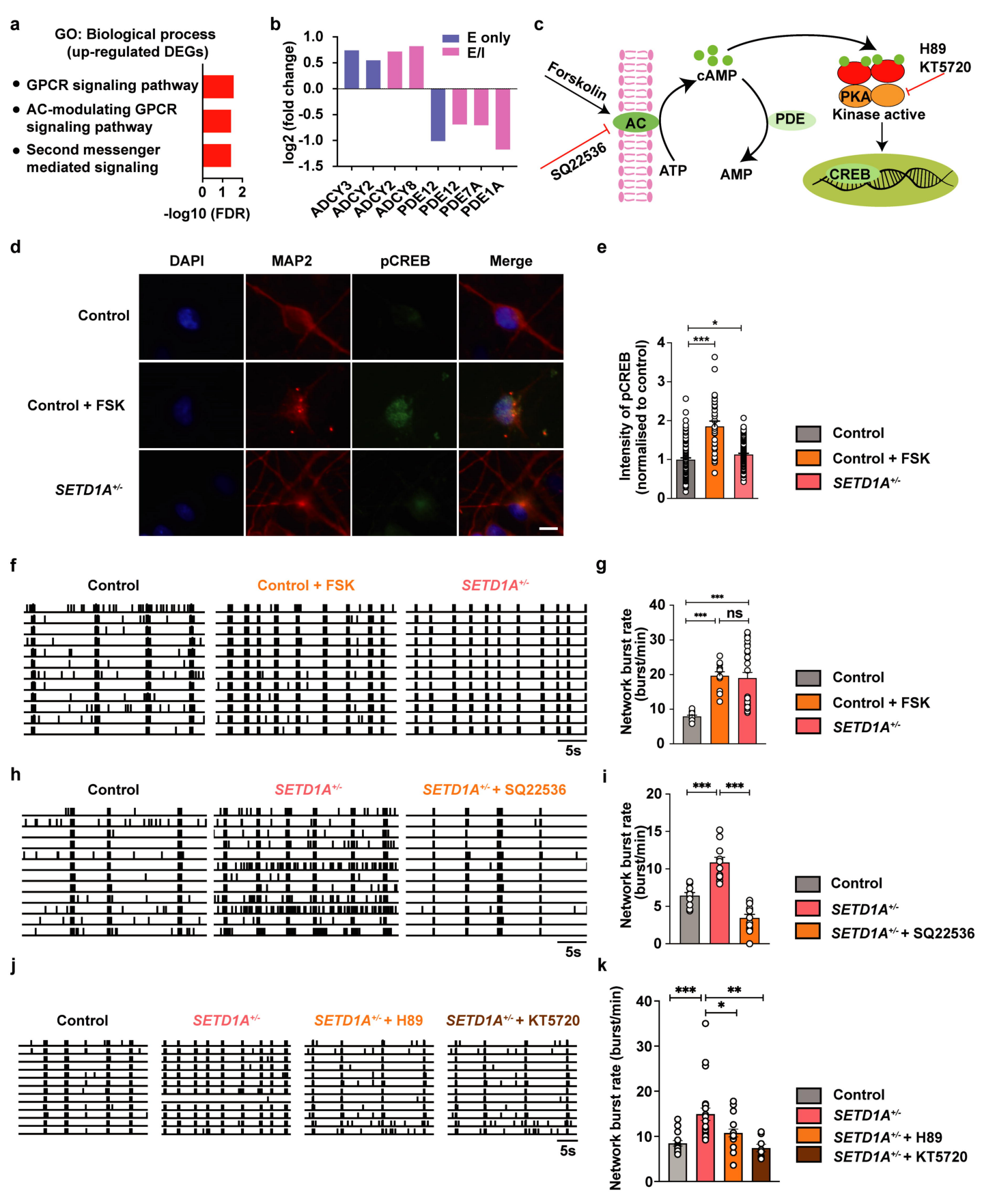
a
GO: Biological process
(up-regulated DEGs)
GPCR signaling pathway
AC-modulating GPCR signaling pathway
Second messenger mediated signaling
0 1 2
-log10 (FDR)
b
E only
E/I
log2 (fold change)
1.0
0.5
0.0
-0.5
-1.0
-1.5
ADCY3
ADCY2
ADCY2
ADCY8
PDE12
PDE12
PDE7A
PDE1A
c
Forskolin
SQ22536
AC
ATP
cAMP
PDE
AMP
H89
KT5720
PKA
Kinase active
CREB
d
DAPI
MAP2
pCREB
Merge
Control
Control + FSK
SETD1A+/-
e
Intensity of pCREB (normalised to control)
Control
Control + FSK
SETD1A+/-
f
Control
Control + FSK
SETD1A+/-
5s
g
Network burst rate (burst/min)
ns
Control
Control + FSK
SETD1A+/-
h
Control
SETD1A+/-
SETD1A+/- + SQ22536
5s
i
Network burst rate (burst/min)
Control
SETD1A+/-
SETD1A+/- + SQ22536
j
Control
SETD1A+/-
SETD1A+/- + H89
SETD1A+/- + KT5720
5s
k
Network burst rate (burst/min)
Control
SETD1A+/-
SETD1A+/- + H89
SETD1A+/- + KT5720